Analysis and Control of Modular Multilevel Converter With Split Energy Storage for Railway Traction Power Conditioner

Peng Guo, *Student Member, IEEE*, Qianming Xu, *Member, IEEE*, Yufei Yue, *Student Member, IEEE*, Fujun Ma, *Member, IEEE*, Zhixing He, *Member, IEEE*, An Luo, *Senior Member, IEEE*, and Josep M. Guerrero, *Fellow, IEEE*

***Abstract*—In this paper, a railway power conditioner (RPC) based on a modular multilevel converter (MMC) with a split supercapacitor energy storage system (SCESS) is studied. In this case, the MMC-SCESS-based RPC could not only provide normal negative-sequence current compensation, but also reduce the impact of power fluctuations caused by the locomotive braking or startup on the electric grid. First, this paper analyzes the power flow patterns and deduces the reference circulating current under different operation modes of the MMC-SCESS-based RPC. Then, the control objectives of the MMC-SCESS-based RPC are divided into two categories—the balance control and the current tracking control. The balance control methods are developed for the submodule capacitor voltages and the state of charge of the supercapacitor, which are associated with the operation modes. To ensure the current tracking performance, a model-predictive direct current control method is presented for the MMC and the bidirectional energy converter. Finally, the effectiveness of the proposed control methods is verified by the experimental results of a downscaled prototype.**

***Index Terms*—Balance control, model-predictive direct current control (MPDCC), modular multilevel converter (MMC), power flow patterns, railway power conditioner (RPC), split supercapacitor energy storage system (SCESS).**

I. Introduction

OVER the years, the high-speed electrified railway has been developed rapidly. Meanwhile, the traction system feature of the locomotives results in some power quality issues such as negative-sequence currents (NSCs), reactive power, harmonic currents, and fluctuant voltages [1]–[4]. Furthermore, the utilization of regenerative braking energy has been becoming a hot topic recently, particularly in China and Japan [5]. Therefore, how to regulate the power quality of the electrified railway and achieve the energy saving for recycling seems to be meaningful.

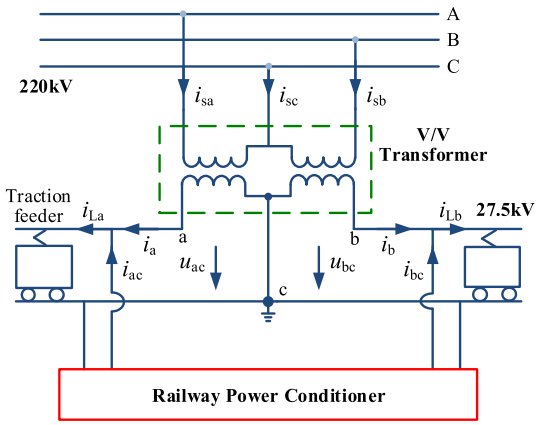

Fig. 1. V/V traction transformer and the RPC.

To solve the problem of the power quality introduced by the electrified railway, various methods have been presented. The solutions could be divided into two categories including optimized power system and adding the compensation equipment. In [6] and [7], different kinds of balance transformers including V/V transformer, Scott transformer, and power electronic transformer are studied for reducing the NSC in a three-phase power system. Meanwhile, the filter equipment such as a static Var compensator [8]–[10], a static synchronous compensator [11], [12], and a hybrid active power filter [13], [14] could be installed in the high-voltage side to compensate reactive current and harmonic currents; however, the cost of electrified railway is also increasing. Then, the idea of railway power conditioner (RPC) is proposed in [15], as shown in Fig. 1, which is placed at the secondary side of the traction transformer and transfers the active power and compensates the reactive power via a back-to-back (BTB) converter. In [16], the multiple BTB in parallel connection is proposed for NSC compensation. The secondary sides of the multiwinding are linked to each BTB output, while the primary sides are linked to the traction arm. Nowadays, a modular multilevel converter (MMC) has attracted significant attention in the field of medium/high-voltage power electronics with

Manuscript received February 21, 2019; revised April 28, 2019; accepted May 11, 2019. Date of publication May 14, 2019; date of current version November 12, 2019. This work was supported in part by the National Natural Science Foundation of China under Grant 51807056 and in part by Hunan Provincial Innovation Foundation for Postgraduate under Grant CX2018B169. Recommended for publication by Associate Editor T. Mishima. *(Corresponding author: Qianming Xu.)*

P. Guo, Q. Xu, Y. Yue, F. Ma, Z. He, and A. Luo are with the College of Electrical and Information Engineering, Hunan University, Changsha 410082, China (e-mail: pengguo92@hnu.edu.cn; hnuxqm@foxmail.com; 14789868647@163.com; mafujun2004@163.com; hezhixingmail@163.com; an_luo@126.com).

J. M. Guerrero is with the Department of Energy Technology, Aalborg University, 9220 Aalborg East, Denmark (e-mail: joz@et.aau.dk).

Color versions of one or more of the figures in this paper are available online at http://ieeexplore.ieee.org.

Digital Object Identifier 10.1109/TPEL.2019.2917065

features of flexible, modularity, and wide voltage level adaptation. Then, many scholars develop an RPC based on the MMC structure. In [17], an RPC characteristic of the two-phase MMC that consists of the full-bridge submodules (SMs) is proposed for NSC compensation. In [18]–[20], the RPCs characteristic based on half-bridge MMC are studied with two arms, three arms, and four arms. In [21], the scholar makes the comparisons for five classical modular RPC topologies and provides the choosing guidelines for special application. It is revealed that the asymmetrical MMC based on half-bridge SMs shows the superior performance in the V/V traction system.

With the growth of the electric load and the interconnection of the regional power system, the concept of the energy storage system (ESS) is initially proposed for dealing with the power quality and the power system stability problem [22]. Nowadays, with the penetration of the renewable source, the ESS is once again to cope with the power fluctuation resulted from the randomness and intermittent nature of renewable energy. So, how to integrate the ESS into the power electronic converter effectively has been studied widely [23]. Among them, the structure of the MMC with a split ESS has become a promising and emerging way [24]. In [25], the scholars make a discussion on the enhancement of performance, reliability, and flexibility of the modular multilevel cascaded converter (MMCC) with a split battery energy storage system (BESS). The BESS can provide the MMCC with satisfactory performance on zero-voltage ride-through. In [26], an energy injection method is proposed to rebalance the ac voltage of grid asymmetries by utilizing the BESS. In [27], the operation modes of the MMC with an integrated BESS are analyzed, and the balance methods for the state of charge (SoC) are developed. A nonisolated dc–dc converter is utilized to link the split BESS to the SM when the direct connection to the SM may decrease the battery lifetime. In [28], a novel balance control method based on the state of health of the recycled batteries is proposed to enhance the output capacity and lifetime of the MMC BESS. From the point of view of the system efficiency [29], the scholar makes a comparison for three kinds of classical MMC topologies with the split BESS. In [30], a hybrid modular multilevel converter (HMMC) with the integrated BESS is proposed, and the control strategies under normal modes and fault modes are studied. A decoupled power method based on the HMMC with a hybrid ESS is presented in [31]. In this configuration, the long-term fluctuant power is compensated by the battery energy, while the short-term fluctuant power is compensated by the supercapacitor energy, which benefits for improving the reliability of the storage elements. Recently, the utilization of the regenerative braking energy of the traction locomotive is gradually attracting more attention when the traditional mechanical brakes and braking resistors may face the challenge of the environmental impact and energy saving. Due to the energy storage characteristic of high-power density, the supercapacitor is more applicable to the utilization of the regenerative braking energy compared to the battery storage [32]. In [33], a simplified mathematical model of the MMC integrated with the supercapacitor energy system is presented, and the control methods for traction motor and energy system balance are validated by the numerical simulations. Although many pieces of literature have made been studied on the MMC with the split ESS, the MMC with a split supercapacitor energy storage system (MMC-SCESS)-based RPC is rarely studied and deserves to be further researched.

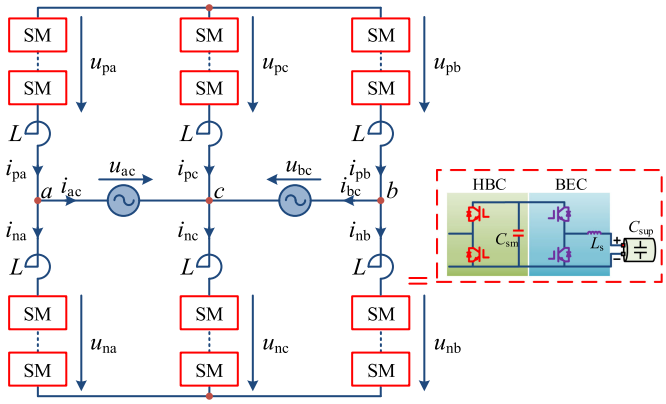

Fig. 2. Main topology of the MMC-SCESS-based RPC.

For this reason, an MMC-SCESS-based RPC is proposed to apply for the railway traction power conditioner with the ability to adapt different operation modes. In the normal operation mode, the MMC-SCESS-based RPC system could compensate the NSC, while in the extended operation mode, the MMC-SCESS-based RPC system could absorb the regenerative braking energy in the braking mode and supply the peak power in the startup mode. The highlight of this paper includes: 1) analysis of the power flow patterns and reference circulating current under different operation modes; and 2) research on control methods, including the balance control and the current tracking control.

The rest of this paper is organized as follows. In Section II, the system configuration and the mathematical model of the MMC-SCESS-based RPC are introduced. Afterward, the operation principle and the power flow of the MMC-SCESS-based RPC under different operation modes are analyzed in Section III. Section IV mainly discusses the control methods of the MMC-SCESS-based RPC. The experiments are carried out to demonstrate the effectiveness of the studied MMC-SCESS-based RPC and the proposed control methods in Section V. Section VI draws the conclusion.

II. System Configuration and Modeling of the MMC-SCESS-Based RPC

The main topology of the MMC-SCESS-based RPC to be discussed is shown in Fig. 2. It contains three phases, and each phase contains two arms, which are connected by inductor L and its internal resistance r. Each arm consists of N series SMs, and each SM consists of the half-bridge converter (HBC) and the supercapacitor, which are connected by bidirectional energy converter (BEC). u_{pj} and u_{nj} $(j = \mathrm{a}, \mathrm{b}, \mathrm{c})$ denote the upper and lower arm voltages, respectively. i_{pj} and i_{nj} denote the upper and lower arm currents, respectively. The midpoints of three phases are connected to the V/V transformer—the midpoint of phase c is connected to the common point of the V/V transformer, while the midpoints of phases a and b are connected to the ends of the V/V transformer. For convenient analysis, the mathematical

model of the MMC-SCESS-based RPC could be divided into two parts incorporating the mathematical model of the MMC and the mathematical model of the BEC. A brief introduction is given in the following section.

First, obeying the direction of voltages and currents shown in Fig. 2, the external dynamic characteristic equation of phase *j* could be deduced as [34], [35]

$$\frac{L}{2}\frac{di_{jc}}{dt} = \frac{(u_{nj} - u_{pj})}{2} - u_{jc} - u_{co} - \frac{r}{2}i_{jc} \tag{1}$$

where u_{jc} and i_{jc} denote the traction feeder voltage and the output current of phase *j*, respectively. u_{co} denotes the common voltage measured between the midpoint of phase c and the midpoint of the virtual dc link, which is supported by the inserted SM capacitor voltages.

In spite of the asymmetric characteristic of the MMC-SCESS-based RPC, the external characteristic equations of three phases are symmetric, meaning that the common voltage u_{co} could be obtained by summing the external characteristic equations of three phases as

$$u_{co} = -\frac{1}{3}\sum_{j=a,b,c} u_{jc} = -\frac{1}{3}(u_{ac} + u_{bc}). \tag{2}$$

Assuming that the SM capacitor voltages are well balanced, the internal dynamic characteristic equation of phase *j* could be deduced as [34], [35]

$$L\frac{di_{zj}}{dt} = \frac{U_{dc}}{2} - \frac{u_{nj} + u_{pj}}{2} - ri_{zj} \tag{3}$$

where U_{dc} and i_{zj} denote the virtual dc-link voltage and the circulating current of phase *j*. In addition, the arm voltage of phase *j* could also be given approximately as follows:

$$\begin{cases} u_{pj} = \sum_{k=1}^{N} s_{pkj}u_{pckj} \approx \frac{N_p}{N}u_{pcj}^{\Sigma} \\ u_{nj} = \sum_{k=1}^{N} s_{nkj}u_{nckj} \approx \frac{N_n}{N}u_{ncj}^{\Sigma} \end{cases} \tag{4}$$

where s_p and s_n denote the upper and lower arm SM switching states, respectively. u_{pc} and u_{nc} denote the upper and lower arm SM capacitor voltages, respectively. u_{pc}^{Σ} and u_{nc}^{Σ} denote the summation of the upper and lower arm SM capacitor voltages, respectively. N_p and N_n indicate the upper and lower arm inserted SM numbers, respectively.

To ensure the energy bidirectional flow with the characteristic of the reliability, it utilizes a bidirectional buck–boost converter to decouple the supercapacitor from the dc-link voltage of the HBC in this paper. Assuming that the converter is always operating in the continuous current mode, the current paths of the BEC under different operation modes are shown in Fig. 3.

There are two kinds of operations, including the energy storage mode and the energy release mode, as shown in Fig. 3(a) and (b), respectively. When the BEC is operating in the energy storage mode, as shown in Fig 3(a), i.e., the energy could flow from the HBC dc link to the supercapacitor, Q_1 is set to the pulsewidth modulation (PWM) state and Q_2 is set to the OFF-state. Inversely, when the BEC is operating in the energy release mode, as shown in Fig 3(b), i.e., the energy flows from the supercapacitor to the HBC dc link, Q_1 is set to the OFF-state and Q_2 is set to the PWM

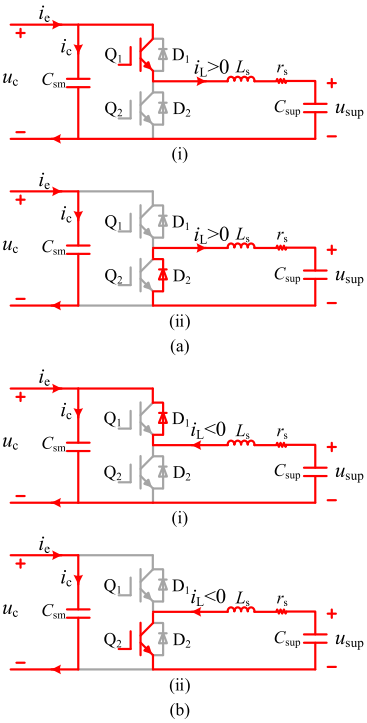

Fig. 3. Current paths of the BEC in the extended operation mode. (a) Energy storage mode: (i) Q_1: ON, Q_2: OFF and (ii) Q_1: OFF, Q_2: OFF. (b) Energy release mode: (i) Q_1: OFF, Q_2: OFF and (ii) Q_1: OFF, Q_2: ON.

state. It is worth to mention that the current paths of Fig. 3(a)(i) and (a)(ii) are identical to those of Fig. 3(b)(i) and (b)(ii), respectively, so the mathematical models of the converter in two modes could be given in a unified expression as

$$\begin{cases} \frac{du_c}{dt} = \frac{1}{C_{sm}}(i_e - Qi_L) \\ \frac{di_L}{dt} = \frac{1}{L_s}(Qu_c - u_{sup} - r_s i_L) \end{cases} \tag{5}$$

where i_e and i_L denote the input current and inductor current, respectively. u_c and u_{sup} denote the SM capacitor voltage and the supercapacitor voltage, respectively. In unified expressions, when $i_L \geq 0$, $Q_1 = Q$ and $Q_2 = 0$, while $i_L < 0$, $Q_2 = (1 - Q)$ and $Q_1 = 0$.

III. Operation Principle and Power Flow Analysis of the MMC-SCESS-Based RPC

For the MMC-SCESS-based RPC, the power flow is closely related to its operation modes, which incorporate the normal operation mode and the extended operation mode. In general, the power flow based on the former mode occurs between the electric grid and the traction locomotive, while the power flow based on the latter mode occurs between the supercapacitor and the traction locomotive. Since the operation modes are associated with the control objectives of the MMC-SCESS-based RPC detailed in Section IV, it is worthwhile first to analyze the power flow. The corresponding processes are presented as follows.

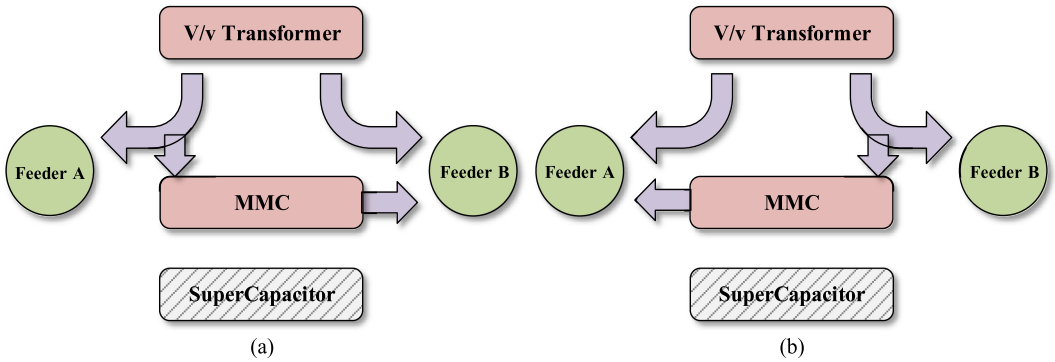

Fig. 4. Power flow of the MMC-SCESS-based RPC under the normal operation mode. (a) $P_{\mathrm{FA}} \le P_{\mathrm{FB}}$. (b) $P_{\mathrm{FA}} > P_{\mathrm{FB}}$.

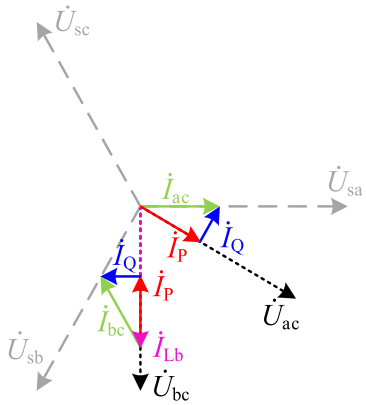

Fig. 5. Compensation principle phasor diagram of the V/V traction system.

A. Normal Operation Mode

If the MMC-SCESS-based RPC is operating in the normal mode, i.e., the supercapacitor does not work, then the MMC system takes responsibility for NSC compensation. In this case, the power flow is depicted in Fig. 4. When the active power required by traction feeder A is lower than that by traction feeder B, the power flow is shown in Fig. 4(a), and the MMC transfers half of the active power difference from the left traction arm to the right one. Conversely, when the active power required by traction feeder A is more than that by traction feeder B, the power flow is shown in Fig. 4(b), and the MMC transfers half of the active power difference from the right traction arm to the left one.

For convenient analysis, we assume that phase b is in full load, while phase a is in no load. According to the compensation principle of the V/V traction system [36], the compensation phasor diagram is depicted in Fig. 5. In this case, the traction feeder voltage and the reference compensation currents could be defined as follows:

$$\begin{cases} u_{\mathrm{ac}} = U_{\mathrm{s}}\sin\left(\omega t + \theta_{\mathrm{ac}}\right) \\ u_{\mathrm{bc}} = U_{\mathrm{s}}\sin\left(\omega t + \theta_{\mathrm{bc}}\right) \end{cases} \tag{6}$$

$$\begin{cases} i_{\mathrm{ac0}}^{\mathrm{ref}} = I_{\mathrm{Q}}\sin\left(\omega t + \theta_{\mathrm{ac}} + \pi/2\right) - I_{\mathrm{P}}\sin\left(\omega t + \theta_{\mathrm{ac}}\right) \\ i_{\mathrm{bc0}}^{\mathrm{ref}} = I_{\mathrm{Q}}\sin\left(\omega t + \theta_{\mathrm{bc}} - \pi/2\right) + I_{\mathrm{P}}\sin\left(\omega t + \theta_{\mathrm{bc}}\right) \end{cases} \tag{7}$$

where U_{s} denotes the amplitude of the traction feeder voltage. I_{P} and I_{Q} denote the amplitudes of the reference active current and the reactive current, respectively. The amplitudes and the phase angles in (6) and (7) should satisfy the following conditions:

$$\begin{cases} I_{\mathrm{Q}} = I_{\mathrm{P}}/\sqrt{3} \\ \theta_{\mathrm{ac}} - \theta_{\mathrm{bc}} = \pi/3. \end{cases} \tag{8}$$

Ignoring the loss of the inductance and resistance in each arm, the instantaneous power expressions of the upper and the lower arm in phase j are given as

$$\begin{cases} P_{\mathrm{p}j} = u_{\mathrm{p}j} i_{\mathrm{p}j} = \left(U_{\mathrm{dc}}/2 - \left(u_{jc} + u_{\mathrm{co}}\right)\right)\left(i_{jc}/2 + i_{zj}\right) \\ P_{\mathrm{n}j} = u_{\mathrm{n}j} i_{\mathrm{n}j} = \left(U_{\mathrm{dc}}/2 + \left(u_{jc} + u_{\mathrm{co}}\right)\right)\left(-i_{jc}/2 + i_{zj}\right). \end{cases} \tag{9}$$

To simplify the deduction, the total instantaneous power of the phase j could be deduced by summing these relations in (9) as

$$P_j = U_{\mathrm{dc}} i_{zj} - \left(u_{jc} + u_{\mathrm{co}}\right) i_{jc} \tag{10}$$

$$P_{\mathrm{a}} = \underbrace{U_{\mathrm{dc}} i_{\mathrm{za}} + \frac{1}{4}U_{\mathrm{s}}I_{\mathrm{P}} - \frac{\sqrt{3}}{12}U_{\mathrm{s}}I_{\mathrm{Q}}}_{\text{dc component}} \underbrace{- \frac{1}{3}U_{\mathrm{s}}I_{\mathrm{Q}}\alpha_1 - \frac{1}{3}U_{\mathrm{s}}I_{\mathrm{P}}\beta_1 + \frac{1}{6}U_{\mathrm{s}}I_{\mathrm{Q}}\alpha_3 + \frac{1}{6}U_{\mathrm{s}}I_{\mathrm{P}}\beta_3}_{\text{ac component}} \tag{11}$$

$$P_{\mathrm{b}} = \underbrace{U_{\mathrm{dc}} i_{\mathrm{zb}} - \frac{1}{4}U_{\mathrm{s}}I_{\mathrm{P}} - \frac{\sqrt{3}}{12}U_{\mathrm{s}}I_{\mathrm{Q}}}_{\text{dc component}} \underbrace{+ \frac{1}{3}U_{\mathrm{s}}I_{\mathrm{Q}}\alpha_2 + \frac{1}{3}U_{\mathrm{s}}I_{\mathrm{P}}\beta_2 - \frac{1}{6}U_{\mathrm{s}}I_{\mathrm{Q}}\alpha_3 - \frac{1}{6}U_{\mathrm{s}}I_{\mathrm{P}}\beta_3}_{\text{ac component}} \tag{12}$$

$$P_{\mathrm{c}} = \underbrace{U_{\mathrm{dc}} i_{\mathrm{zc}} + \frac{\sqrt{3}}{6}U_{\mathrm{s}}I_{\mathrm{Q}}}_{\text{dc component}} \underbrace{- \frac{1}{6}U_{\mathrm{s}}I_{\mathrm{Q}}\alpha_1 - \frac{1}{6}U_{\mathrm{s}}I_{\mathrm{P}}\beta_1 + \frac{1}{6}U_{\mathrm{s}}I_{\mathrm{Q}}\alpha_2 + \frac{1}{6}U_{\mathrm{s}}I_{\mathrm{P}}\beta_2}_{\text{ac component}} \tag{13}$$

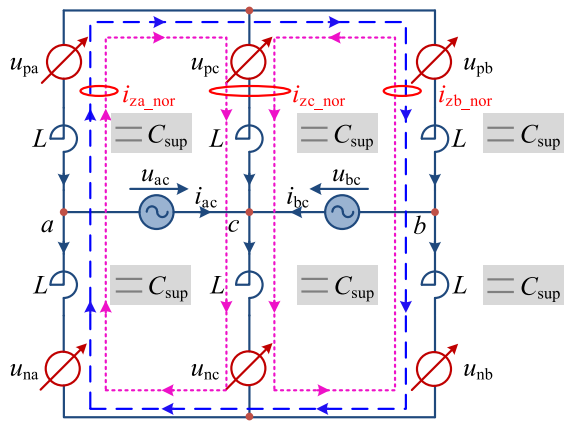

Fig. 6. Characteristic of the circulating current under the normal operation mode.

with

$$\alpha_1 = \sin(2\omega t + 2\theta_{ac}),\ \alpha_2 = \sin(2\omega t + 2\theta_{bc}),$$
$$\alpha_3 = \sin(2\omega t + \theta_{ac} + \theta_{bc})$$
$$\beta_1 = \cos(2\omega t + 2\theta_{ac}),\ \beta_2 = \cos(2\omega t + 2\theta_{bc}),$$
$$\beta_3 = \cos(2\omega t + \theta_{ac} + \theta_{bc}).$$

Substituting (2) and (6)–(8) into (10), after a series of the mathematical operations, the three-phase instantaneous power expressions could be deduced as shown in (11)–(13). In order to ensure stable operation of the MMC system, the dc component of the total instantaneous power on each phase should be kept as zero, which benefits for balancing the SM capacitor voltages. Hence, the reference circulating currents in the normal operation mode could be deduced as follows:

$$\begin{cases} i_{za\_nor} = \frac{1}{U_{dc}}\left(-\frac{1}{4}U_s I_P + \frac{\sqrt{3}}{12}U_s I_Q\right) \\ i_{zb\_nor} = \frac{1}{U_{dc}}\left(\frac{1}{4}U_s I_P + \frac{\sqrt{3}}{12}U_s I_Q\right) \\ i_{zc\_nor} = \frac{1}{U_{dc}}\left(-\frac{\sqrt{3}}{6}U_s I_Q\right). \end{cases} \tag{14}$$

According to (14), the three-phase circulating currents are composed of active circulating current and reactive circulating current components. The former is stimulated by transferring the active power and flows only between phases a and b, as shown by the blue dotted line in Fig. 6, while the latter is stimulated by compensating the reactive power and flows among three phases, as shown by the pink dotted line in Fig. 6.

B. Extended Operation Mode

If the MMC-SCESS-based RPC is operating in the extended mode, such as the braking or startup mode of the traction locomotive, then the supercapacitor could be assessed to reduce the impact of power fluctuations on the electrical grid by energy storage or energy release. In this case, the power flow is depicted in Fig. 7. When the locomotive is operating in the startup mode, the instantaneous launch energy could be provided by the supercapacitor, as shown in Fig. 7(a). When the locomotive is operating in the braking mode, the regenerative braking energy could be feedback to the supercapacitor, as shown in Fig. 7(b).

To simplify the analysis, we assume that only one locomotive is in the braking mode, and the regenerative braking power remains constant. According to (7), the reference compensation currents could be defined as follows:

$$\begin{cases} i_{ac}^{ref} = 0 \\ i_{bc}^{ref} = -I_P \sin(\omega t + \theta_{bc}). \end{cases} \tag{15}$$

Taking the braking mode as an example, because phase a does not participate in the transfer of active power, as shown in Fig. 8(a), the regenerative braking energy will be fully absorbed by the supercapacitor of phases b and c, which consequently results in a significant difference in the SoC between phase b (phase c) and phase a. In order to make full use of the storage capacity of the supercapacitor, the circulating current injection method should be introduced to reduce the phase SoC difference.

First, we define a virtual circulating current i_{vz}, which is utilized for charging supercapacitor but cannot be measured. In order to deduce the expression of i_{vz}, the total instantaneous power expressions of phases b and c could be given as follows:

$$\begin{cases} P_b = -U_{dc} i_{vzb} - \frac{1}{2} u_{bc} i_{bc} \\ P_c = -U_{dc} i_{vzc} - \frac{1}{2} u_{bc} i_{bc}. \end{cases} \tag{16}$$

Substituting (6) and (15) into (16) yields

$$\begin{cases} P_b = \underbrace{-U_{dc} i_{vzb} + \frac{1}{4}U_s I_P}_{\text{dc component}} \underbrace{-\frac{1}{4}U_s I_P \cos(2\omega t + \theta_{bc})}_{\text{ac component}} \\ P_c = \underbrace{-U_{dc} i_{vzc} + \frac{1}{4}U_s I_P}_{\text{dc component}} \underbrace{-\frac{1}{4}U_s I_P \cos(2\omega t + \theta_{bc})}_{\text{ac component}}. \end{cases} \tag{17}$$

For the stable operation of the MMC, the expression for the virtual circulating currents should satisfy the following relations:

$$i_{vzb} = i_{vzc} = \frac{U_s I_P}{4U_{dc}}. \tag{18}$$

Actually, the virtual circulating currents could be decomposed into two terms:

$$\begin{cases} i_{vzb} = i_{zb} + \bar{i}_{vzb} \\ i_{vzc} = i_{zc} + \bar{i}_{vzc} \end{cases} \tag{19}$$

where i_{zb} and i_{zc} denote the injected circulating currents, while $\bar{i}_{vzb}$ and $\bar{i}_{vzc}$ denote the corrected virtual circulating currents. To reduce the phase difference of the SoC, the regenerative braking energy should be distributed symmetrically on the three phases, as shown in Fig. 8(b), that is,

$$\bar{i}_{vzb} = \bar{i}_{vzc} = i_{za}. \tag{20}$$

According to (18)–(20), the reference injected circulating currents are deduced as follows:

$$\begin{cases} i_{za\_ext} = -\frac{U_s I_P}{6U_{dc}} \\ i_{zb\_ext} = \frac{U_s I_P}{12U_{dc}} \\ i_{zc\_ext} = \frac{U_s I_P}{12U_{dc}}. \end{cases} \tag{21}$$

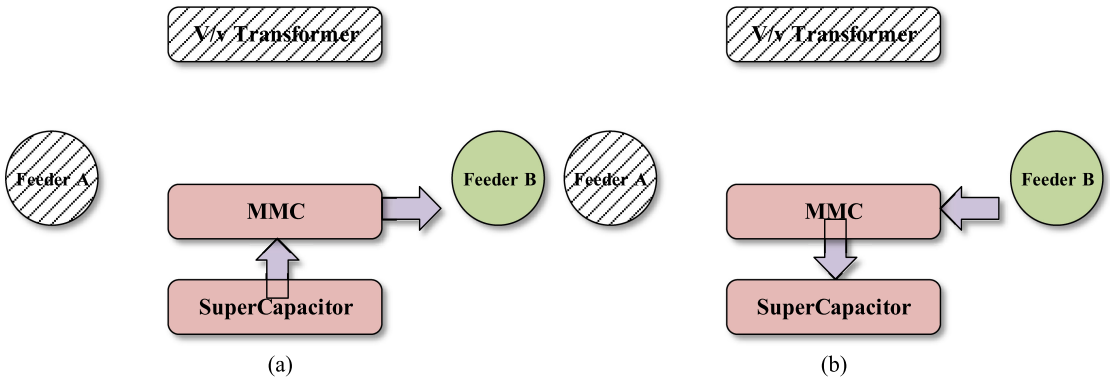

Fig. 7. Power flow of the MMC-SCESS-based RPC under the extended operation mode. (a) Energy release. (b) Energy storage.

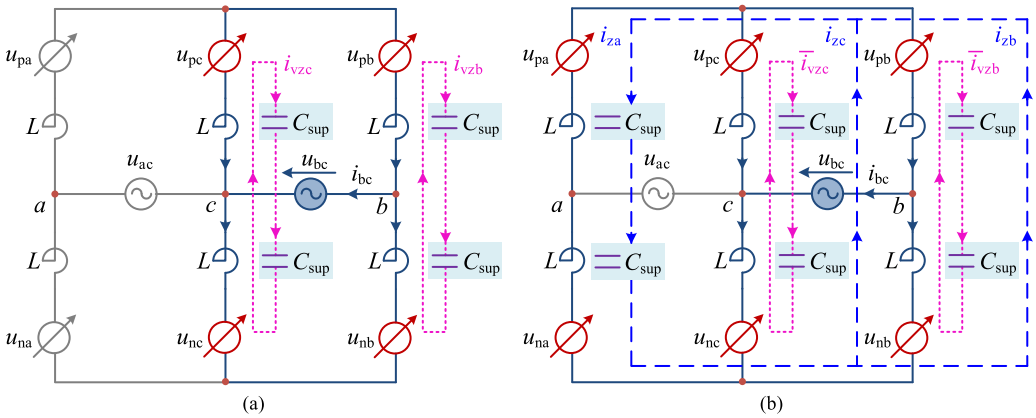

Fig. 8. Characteristic of the circulating current under the energy storage. (a) Without circulating current injection. (b) With circulating current injection.

Similarly, when the traction locomotive is operating in the startup mode, the reference injected circulating currents for reducing the difference in the SoC between phase b (phase c) and phase a could be deduced similarly and do not cover again. Actually, the expressions of the reference injected circulating currents in the startup mode are the same as that in the braking mode, but the sign of the reference amplitude of the active current I_{P} should be reversed.

IV. Control Methods of the MMC-SCESS-Based RPC

A. Control Objectives of the MMC-SCESS-Based RPC

The main control objectives of the MMC-SCESS system are associated with the operation modes. On the one hand, when the MMC-SCESS-based RPC is operating in the normal mode, i.e., for the NSC compensation, the control objectives contain three parts: reference compensation current tracking, reference circulating current tracking, and SM capacitor voltage balancing. On the other hand, when the MMC-SCESS-based RPC is operating in the extended mode, i.e., for energy storage or energy release, the control objectives contain four parts—reference compensation current tracking, reference circulating current tracking, supercapacitor SoC balancing, and SM capacitor voltages balancing. For the sake of simplicity, the control objectives are divided into two categories as follows.

1) *Balance control:* When the MMC-SCESS-based RPC is operating in the normal mode, the balance control mainly contains the total voltage balance, the phase voltage balance, the arm voltage balance, and the individual voltage balance. When the MMC-SCESS-based RPC is operating in the extended mode, the balance control mainly contains the phase SoC balance, the arm SoC balance, and the individual SoC balance. It is worth to mention that the individual voltage balance in the extended mode could be ensured by the BEC controller, which will be introduced in Section IV-C.
2) *Current tracking control of the MMC and the BEC:* The current tracking control of the MMC incorporates the compensation current tracking and the circulating current tracking, which is regardless of the operation modes. When the MMC-SCESS-based RPC is operating in the extended mode, the BEC controller not only realizes the bidirectional energy flow, but also has to retain the SM capacitor voltage balance around the reference value, which could be achieved by manipulating the inductor current directly.

B. Balance Control for the MMC-SCESS-Based RPC

When the MMC-SCESS-based RPC is operating in the normal compensation mode, the purpose of the balance control is to prevent the SM capacitor voltages from divergence due to the unavoidable power difference of the SMs. The detailed voltage balance methods are discussed as follows.

1) Total power balance control: Define $P_{\mathrm{p}j}$ and $P_{\mathrm{n}j}$ to represent the power of the upper arm and the lower arm, respectively. The expressions are given as follows:

$$\begin{cases} P_{\mathrm{p}j} = \frac{1}{2}\sum_{k=1}^{N} u_{\mathrm{pc}kj}^2 \\ P_{\mathrm{n}j} = \frac{1}{2}\sum_{k=1}^{N} u_{\mathrm{nc}kj}^2. \end{cases} \tag{22}$$

As presented in (23), the reference active power for total power balance control could be obtained via the proportional-integral (PI) controller, as follows:

$$P_{\mathrm{total}}^{\mathrm{ref}} = k_{\mathrm{p1}}\left(\frac{1}{2}NU_{\mathrm{cref}}^2 - \frac{1}{6}\sum_{j=\mathrm{a,b,c}}\left(P_{\mathrm{p}j}+P_{\mathrm{n}j}\right)\right) + k_{i1}\int\left(\frac{1}{2}NU_{\mathrm{cref}}^2 - \frac{1}{6}\sum_{j=\mathrm{a,b,c}}\left(P_{\mathrm{p}j}+P_{\mathrm{n}j}\right)\right) \tag{23}$$

where U_{cref} represents the reference SM capacitor voltage. Hence, the amplitude of reference fundamental current is deduced as follows:

$$I_{\mathrm{total}}^{\mathrm{ref}} = \frac{2P_{\mathrm{total}}^{\mathrm{ref}}}{U_{\mathrm{s}}}. \tag{24}$$

2) Phase power balance control: According to (9), the summation of the upper and lower arm voltages only contains the dc components, i.e., the imbalance of phase power could be eliminated by injecting the dc circulating current. Because the total power balance is ensured by (24), the control degrees of freedom of phase power control are actually only two, i.e., as long as the arbitrary two-phase circulating current is controlled, the three-phase power deviation could be eliminated. So, the reference phase power deviations are given as

$$\begin{cases} P_{\mathrm{suma}}^{\mathrm{ref}} = k_{\mathrm{p2}}\left(P_{\mathrm{a}} - NU_{\mathrm{cref}}^2\right) + k_{i2}\int\left(P_{\mathrm{a}} - NU_{\mathrm{cref}}^2\right) \\ P_{\mathrm{sumb}}^{\mathrm{ref}} = k_{\mathrm{p2}}\left(P_{\mathrm{b}} - NU_{\mathrm{cref}}^2\right) + k_{i2}\int\left(P_{\mathrm{b}} - NU_{\mathrm{cref}}^2\right) \end{cases} \tag{25}$$

where P_j denotes the summation of $P_{\mathrm{p}j}$ and $P_{\mathrm{n}j}$. The reference dc circulating currents for phase power balance control are calculated correspondingly as

$$\begin{cases} I_{\mathrm{suma}}^{\mathrm{ref}} = P_{\mathrm{suma}}^{\mathrm{ref}}/U_{\mathrm{dc}} \\ I_{\mathrm{sumb}}^{\mathrm{ref}} = P_{\mathrm{sumb}}^{\mathrm{ref}}/U_{\mathrm{dc}}. \end{cases} \tag{26}$$

3) Arm power balance control: According to (9), the difference between the upper and lower arm voltages only contains the fundamental components, i.e., the imbalance of the arm power could be eliminated by injecting the fundamental circulating current. The reference arm power deviations are given as

$$\begin{cases} P_{\mathrm{diffa}}^{\mathrm{ref}} = k_{\mathrm{p3}}\left(P_{\mathrm{na}} - P_{\mathrm{pa}}\right) + k_{i3}\int\left(P_{\mathrm{na}} - P_{\mathrm{pa}}\right) \\ P_{\mathrm{diffb}}^{\mathrm{ref}} = k_{\mathrm{p3}}\left(P_{\mathrm{nb}} - P_{\mathrm{pb}}\right) + k_{i3}\int\left(P_{\mathrm{nb}} - P_{\mathrm{pb}}\right) \\ P_{\mathrm{diffc}}^{\mathrm{ref}} = k_{\mathrm{p3}}\left(P_{\mathrm{nc}} - P_{\mathrm{pc}}\right) + k_{i3}\int\left(P_{\mathrm{nc}} - P_{\mathrm{pc}}\right). \end{cases} \tag{27}$$

Because the control degrees of freedom of arm power control are three, fundamental positive-sequence circulating currents and fundamental negative-sequence circulating currents are needed to be injected simultaneously, as shown in (28), which contains four controllable states including positive-sequence amplitude $I_{\mathrm{z}+}$, positive-sequence phase angle θ_+, negative-sequence amplitude $I_{\mathrm{z}-}$, and negative-sequence phase angle θ_-

$$\begin{cases} i_{\mathrm{diffa}}^{\mathrm{ref}} = I_{\mathrm{z}+}\sin\left(\omega t+\theta_+\right) + I_{\mathrm{z}-}\sin\left(\omega t+\theta_-\right) \\ i_{\mathrm{diffb}}^{\mathrm{ref}} = I_{\mathrm{z}+}\sin\left(\omega t+\theta_+ - 2\pi/3\right) \\ \qquad\qquad + I_{\mathrm{z}-}\sin\left(\omega t+\theta_- - 4\pi/3\right) \\ i_{\mathrm{diffc}}^{\mathrm{ref}} = I_{\mathrm{z}+}\sin\left(\omega t+\theta_+ - 4\pi/3\right) \\ \qquad\qquad + I_{\mathrm{z}-}\sin\left(\omega t+\theta_- - 2\pi 3\right). \end{cases} \tag{28}$$

The arm power deviations introduced by injecting the circulating current are shown in (29), and the derivation in detail is listed in Appendix I:

$$\begin{cases} P_{\mathrm{diffa}} = \frac{1}{\sqrt{3}}U_{\mathrm{s}}I_{\mathrm{z}+}\cos\theta_+ + \frac{1}{\sqrt{3}}U_{\mathrm{s}}I_{\mathrm{z}-}\cos\theta_- \\ P_{\mathrm{diffb}} = \frac{1}{\sqrt{3}}U_{\mathrm{s}}I_{\mathrm{z}+}\cos\theta_+ + \frac{1}{\sqrt{3}}U_{\mathrm{s}}I_{\mathrm{z}-}\cos\left(\theta_- - 2\pi/3\right) \\ P_{\mathrm{diffc}} = \frac{1}{\sqrt{3}}U_{\mathrm{s}}I_{\mathrm{z}+}\cos\theta_+ + \frac{1}{\sqrt{3}}U_{\mathrm{s}}I_{\mathrm{z}-}\cos\left(\theta_- - 4\pi/3\right). \end{cases} \tag{29}$$

Setting θ_+ to be zero and substituting reference arm power deviations into (29), the value of $I_{\mathrm{z}+}$, $I_{\mathrm{z}-}$, and θ_- could be deduced as follows:

$$\begin{cases} I_{\mathrm{z}+} = \sqrt{3}P_{\mathrm{diffcm}}/U_s \\ I_{\mathrm{z}-} = \sqrt{d_1^2+d_2^2} \\ \cos\theta_- = d_1/\sqrt{d_1^2+d_2^2} \\ \sin\theta_- = d_2/\sqrt{d_1^2+d_2^2} \end{cases} \tag{30}$$

with

$$\begin{cases} d_1 = \sqrt{3}\left(P_{\mathrm{diffa}}^{\mathrm{ref}} - P_{\mathrm{diffcm}}^{\mathrm{ref}}\right)/U_{\mathrm{s}} \\ d_2 = 2\left(P_{\mathrm{diffb}}^{\mathrm{ref}} - P_{\mathrm{diffcm}}^{\mathrm{ref}}\right)/U_{\mathrm{s}} + \left(P_{\mathrm{diffa}}^{\mathrm{ref}} - P_{\mathrm{diffcm}}^{\mathrm{ref}}\right)/U_{\mathrm{s}} \\ P_{\mathrm{diffcm}}^{\mathrm{ref}} = \left(P_{\mathrm{diffa}}^{\mathrm{ref}} + P_{\mathrm{diffb}}^{\mathrm{ref}} + P_{\mathrm{diffc}}^{\mathrm{ref}}\right)/3. \end{cases}$$

4) Individual SM power balance control: The difference among the individual SM power in the same arm could be eliminated by the independent PI controller or *sorting algorithm* [37]. As the former method may increase the design complexity of the distributed controller, the latter method is utilized to balance the individual SM power and determines the final switching states in this paper.

When the MMC-SCESS-based RPC is operating in the extended mode, the above balance control methods are also suitable for supercapacitor SoC balance including phase SoC balance and arm SoC balance and do not cover again. It is noted that the SM capacitor voltage balance in the extended mode is ensured by the BEC controller (introduced in Section IV-C); the individual SoC balance in the same arm could be achieved

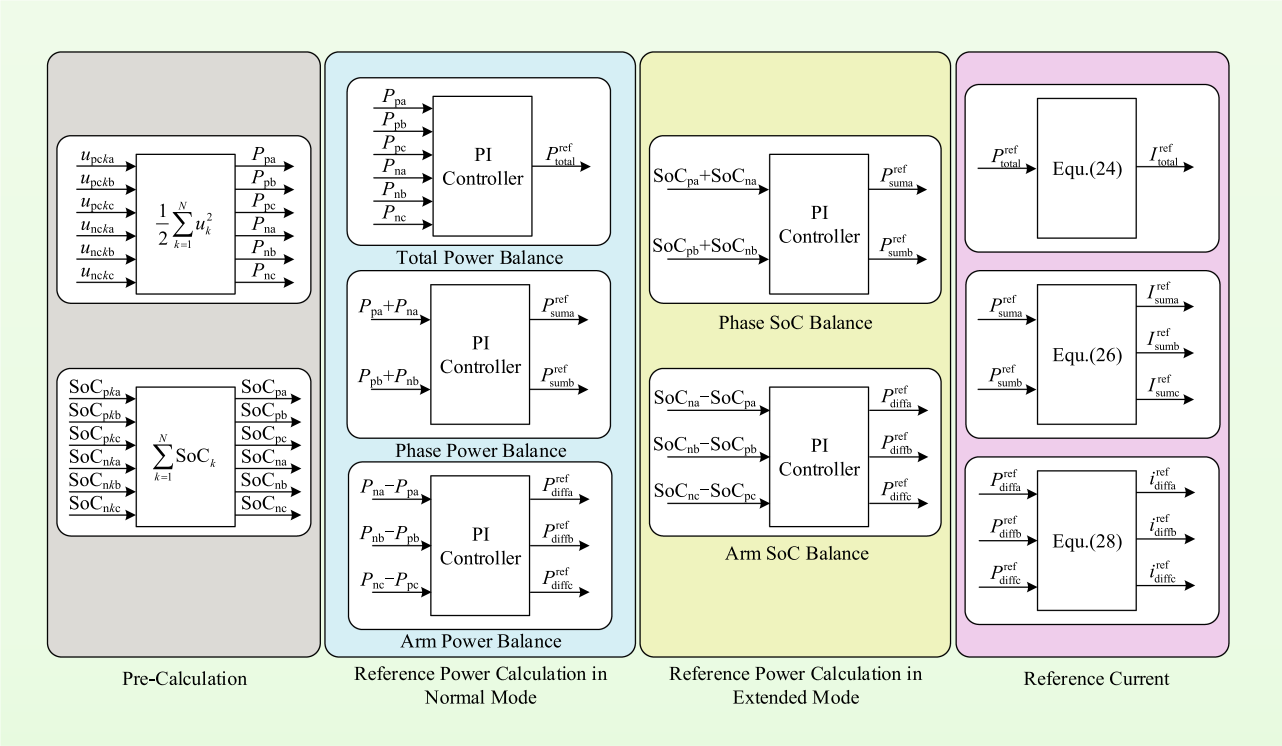

Fig. 9. Balance control methods under different operations modes.

indirectly by sorting the corrected SMs capacitor voltages expressed as

$$\begin{cases} u_{\mathrm{pc}kj\_\mathrm{corrected}} = u_{\mathrm{pc}kj} + \lambda\left(\mathrm{SoC_{pk}}j - \frac{1}{N}\sum_{k=1}^{N}\mathrm{SoC_{p}}kj\right) \\ u_{\mathrm{nc}kj\_\mathrm{corrected}} = u_{\mathrm{nc}kj} + \lambda\left(\mathrm{SoC_{nk}}j - \frac{1}{N}\sum_{k=1}^{N}\mathrm{SoC_{p}}kj\right) \end{cases} \tag{31}$$

where $u_{\mathrm{pc}kj\_\mathrm{corrected}}$ and $u_{\mathrm{nc}kj\_\mathrm{corrected}}$ denote the upper and lower arm corrected SM capacitor voltages, respectively, and λ denotes the correction coefficient.

Therefore, the diagram of the balance control methods under different operations modes is shown in Fig. 9.

C. Model-Predictive Direct Current Control for the MMC-SCESS-Based RPC

In this paper, a model-predictive direct current control (MPDCC) method is utilized for the current tracking of the MMC-SCESS-based RPC. Since the MMC-SCESS-based RPC incorporates two independent parts of the MMC and the BEC, the MPDCC method is designed separately for a reduced computation, and the detailed implementation process is as follows.

First, according to (1)–(5), the continuous mathematical model of the MMC in phase *j* and the arbitrary BEC could be organized as follows:

$$\begin{bmatrix} \dot{\boldsymbol{x}} \\ \dot{\boldsymbol{x}}_{\mathbf{e}} \end{bmatrix} = \begin{bmatrix} \boldsymbol{A}\boldsymbol{x} \\ \boldsymbol{A'}\boldsymbol{x}_{\mathbf{e}} \end{bmatrix} + \begin{bmatrix} \boldsymbol{B} \\ \boldsymbol{B'} \end{bmatrix}. \tag{32}$$

The state variables $\boldsymbol{x} = [i_{jc}\, i_{zj}]^{\mathrm{T}}$ are used to describe the MMC and consist of the output current and the circulating current, while the state variables $\boldsymbol{x}_{\mathbf{e}} = [u_{\mathrm{c}}\, i_{\mathrm{L}}]^{\mathrm{T}}$ are used to describe the BEC and consist of the SM capacitor voltage and the inductor current. The matrices $\boldsymbol{A}$, $\boldsymbol{B}$, $\boldsymbol{A'}$, and $\boldsymbol{B'}$ are listed in Appendix II.

Assuming that the slope of state variables keeps constant in one control period, an approximate discrete method, known as *forward Euler method*, could be introduced to discretize (32), yielding

$$\begin{bmatrix} \boldsymbol{x}\,(\boldsymbol{k}+1) \\ \boldsymbol{x}_e\,(\boldsymbol{k}+1) \end{bmatrix} = \begin{bmatrix} \boldsymbol{G}\boldsymbol{x}\,(\boldsymbol{k}) \\ \boldsymbol{G'}\boldsymbol{x}_e\,(\boldsymbol{k}) \end{bmatrix} + \begin{bmatrix} \boldsymbol{H} \\ \boldsymbol{H'} \end{bmatrix} \tag{33}$$

where the matrices $\boldsymbol{G}, \boldsymbol{H}, \boldsymbol{G'}$, and $\boldsymbol{H'}$ are also listed in Appendix II.

Then, the control objectives of the MMC-SCESS-based RPC associated with the output current, the circulating current, and the inductor current are mapped into the cost functions J and J_{e}, respectively, given as follows:

$$\begin{bmatrix} J \\ J_{\mathrm{e}} \end{bmatrix} = \begin{bmatrix} |\boldsymbol{x}^{\mathbf{ref}}(k+1) - \boldsymbol{x}(k+1)|_{\boldsymbol{W}} \\ |i_{\mathrm{L}}^{\mathrm{ref}}(k+1) - i_{\mathrm{L}}(k+1)| \end{bmatrix}. \tag{34}$$

For the MMC, $\boldsymbol{x}(k+1) = [i_{jc}(k+1)\, i_{zj}(k+1)]^{\mathrm{T}}$ denotes the prediction value of state variables and is calculated by (33). $\boldsymbol{x}^{\mathbf{ref}}(k+1) = [i_{jc}^{\mathrm{ref}}(k+1) i_{zj}^{\mathrm{ref}}(k+1)]^{\mathrm{T}}$ denotes the reference value of state variables. The matrix $\boldsymbol{W} = \mathrm{diag}([w_1, w_2])$ is utilized to penalize the tracking error of the output current and the circulating current. The design method for weighting matrix could be referred to [38]. When the MMC-SCESS-based RPC is

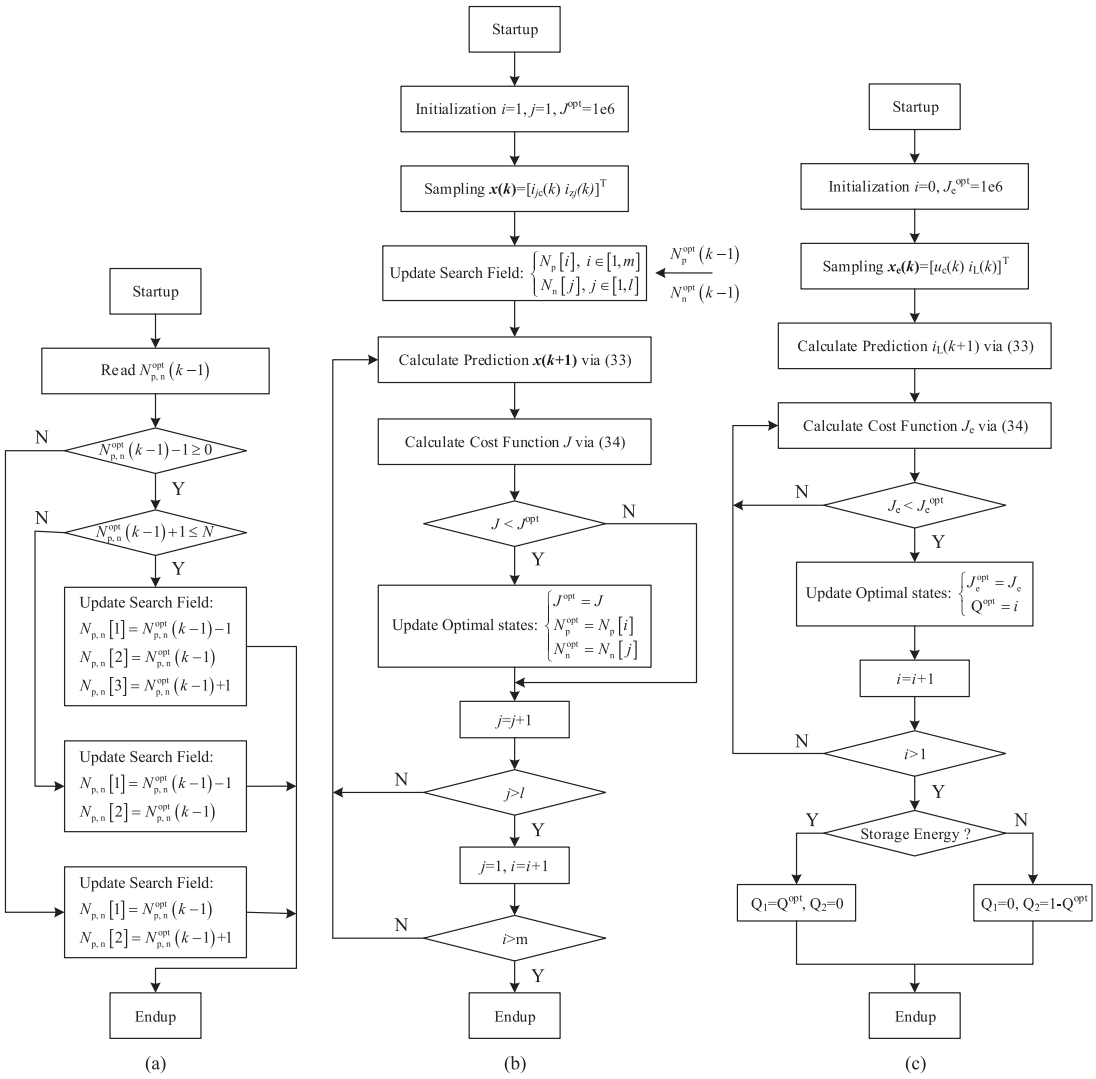

Fig. 10. Flowcharts of the MPDCC for the MMS-SCESS-based RPC. (a) Update method for current search field of the MMC. (b) MPDCC for the MMC. (c) MPDCC for the BEC.

operating in the normal compensation mode, the reference compensation current $i_{jc}^{\mathrm{ref}}(k+1)$ could be given by synthesizing (7) and (24), while the reference circulating currents $i_{zj}^{\mathrm{ref}}(k+1)$ could be given by (14), (26), and (28). When the MMC-SCESS-based RPC is operating in the extended mode, the reference compensation current $i_{jc}^{\mathrm{ref}}(k+1)$ could be given by (15), while the reference circulating currents $i_{zj}^{\mathrm{ref}}(k+1)$ could be given by (21), (26), and (28).

For the BEC, $i_L^{\mathrm{ref}}(k+1)$ and $i_L(k+1)$ denote the prediction and reference of the inductor current, respectively. To improve the steady performance and antidisturbance, the outer voltage controller is introduced to fine-tune the reference inductor current as expressed in the following:

$$i_{\mathrm{L}}^{\mathrm{ref}}=\frac{P_{\mathrm{e}}^{\mathrm{ref}}}{6Nu_{\mathrm{sup}}}+\sigma\left(U_{\mathrm{cref}}-u_{\mathrm{c}}\right) \tag{35}$$

where $P_{\mathrm{e}}^{\mathrm{ref}}$ denotes the reference power for energy storage or energy release and σ denotes the fine-tuning coefficient.

Due to the continuity of the state variables, the current search field of the MMC could be limited to the set, in which the elements are adjacent to the previous optimal inserted number [39]–[41]. So, in this paper, the concept of adjacent search is also applied to reduce the computation. The flowchart of the update method for the current search field is shown in Fig. 10(a). Noting that the number for the current inserted number $N_{\mathrm{p,\ n}}$ to be evaluated is at most three, i.e., nine inserted number combinations $[N_{\mathrm{p}}\ N_{\mathrm{n}}]$ are required to be evaluated for each phase in each sampling value. The flowcharts of the MPDCC for the MMC and the BEC are shown in Fig. 10(b) and (c), respectively. For each combination of inserted number $[N_{\mathrm{p}}\ N_{\mathrm{n}}]$ in search field for the MMC and each switching states Q for the BEC, the state variables at instant $k+1$ are predicted by using the discrete model (33). Then, the cost functions are calculated according to (34). Finally, the optimal inserted number $[N_{\mathrm{p}}^{\mathrm{opt}}\ N_{\mathrm{n}}^{\mathrm{opt}}]$ that minimizes the cost function J could be obtained and further transferred into the optimal switching states $[\mathbf{s}_{\mathrm{p}}^{\mathrm{opt}}\ \mathbf{s}_{\mathrm{n}}^{\mathrm{opt}}]$ for the MMC via the *sorting algorithm*, while the optimal switching

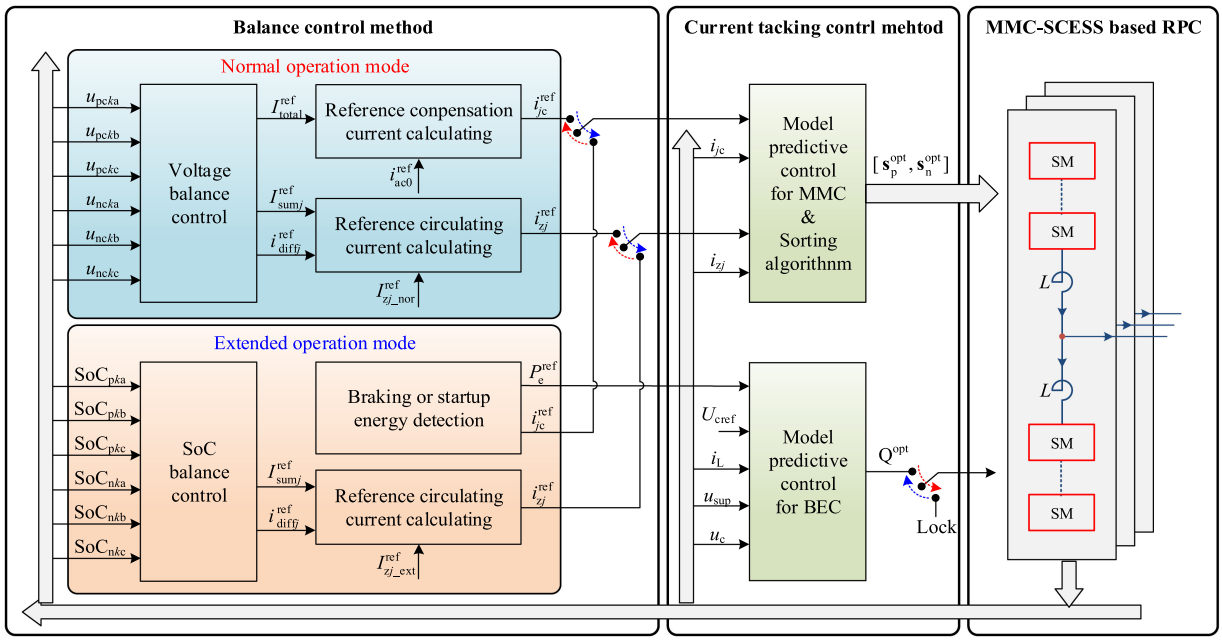

Fig. 11. Overall control block diagram of the MMC-SCESS-based RPC.

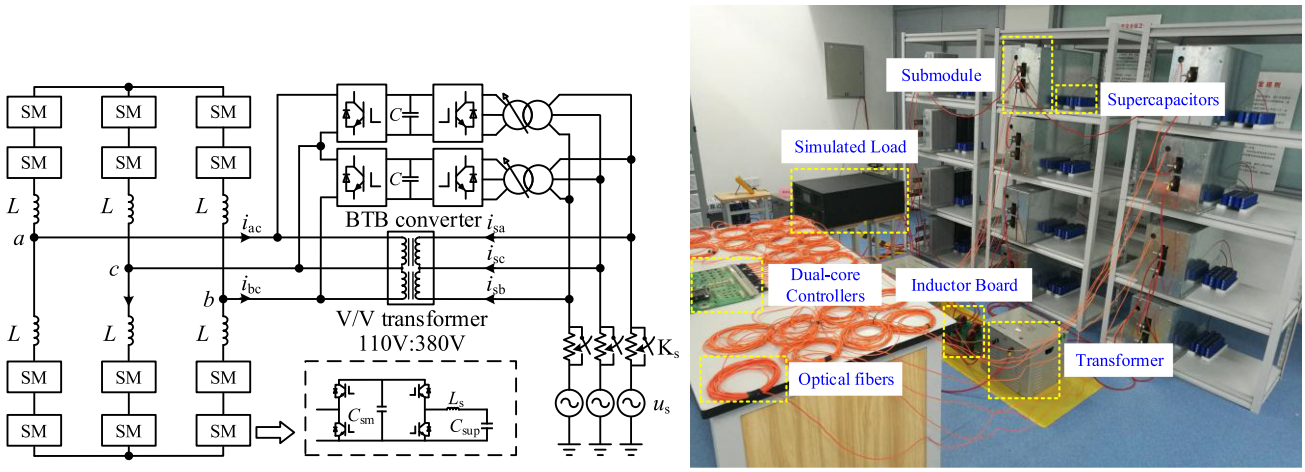

Fig. 12. Experimental setup of the MMC-SCESS-based RPC. (a) Schematic of the downscaled prototype system. (b) Picture of the downscaled prototype system.

states Q^{opt} that minimizes the cost function J_{e} could also be selected to apply for the BEC.

Combining the balance control methods in different operation modes and the MPDCC methods for the current tracking, the overall control block diagram of the MMC-SCESS-based RPC is shown in Fig. 11.

V. Experimental Results

In order to test experimentally the basic functionalities of the studied MMC-SCESS-based RPC and verify the effectiveness of the proposed control methods, experiments of the downscaled prototype are designed and constructed in the laboratory, as shown in Fig. 12. The main parameters are listed in Table I. The design principle of parameters could refer to [21] and [29].

The main circuit consists of the MMC-SCESS, the simulated load, and the V/V traction transformer. First, the MMC-SCESS contains three phases, and each phase contains two arms. Each arm is equipped with two SMs, and each SM consists of the HBC, the BEC, and the supercapacitor. In general, the supercapacitor has low cell voltage, typical 2.7 V, so the supercapacitors are connected in series to demand the relatively high voltage (such as 72 V in this paper), and an additional balance circuit is used to ensure the balance among the supercapacitors connected in series. Then, a BTB three-phase to two-phase two-level converter is used to simulate the different operation modes of the

TABLE I
MAIN PARAMETERS OF THE MMC-SCESS-BASED RPC IN THE DOWNSCALED PROTOTYPE

Parameters	Value	Parameters	Value
Locomotive capacity P	5 kW	Arm inductance L	1 mH
Traction supply voltage u_{ac}, u_{bc}	110 V	Supercapacitor C_{sup}	6 F
Braking/Startup Power P_{bs}	2.5 kW	Filter inductance L_s	10 mH
Rated SMs capacitor voltage U_{cref}	90 V	Initial Supercapacitor SoC	50 %
Number of SMs per arm N	2	Sampling time T_s	100 μs
SM capacitance C_{sm}	10 mF	Operation frequency f	50 Hz

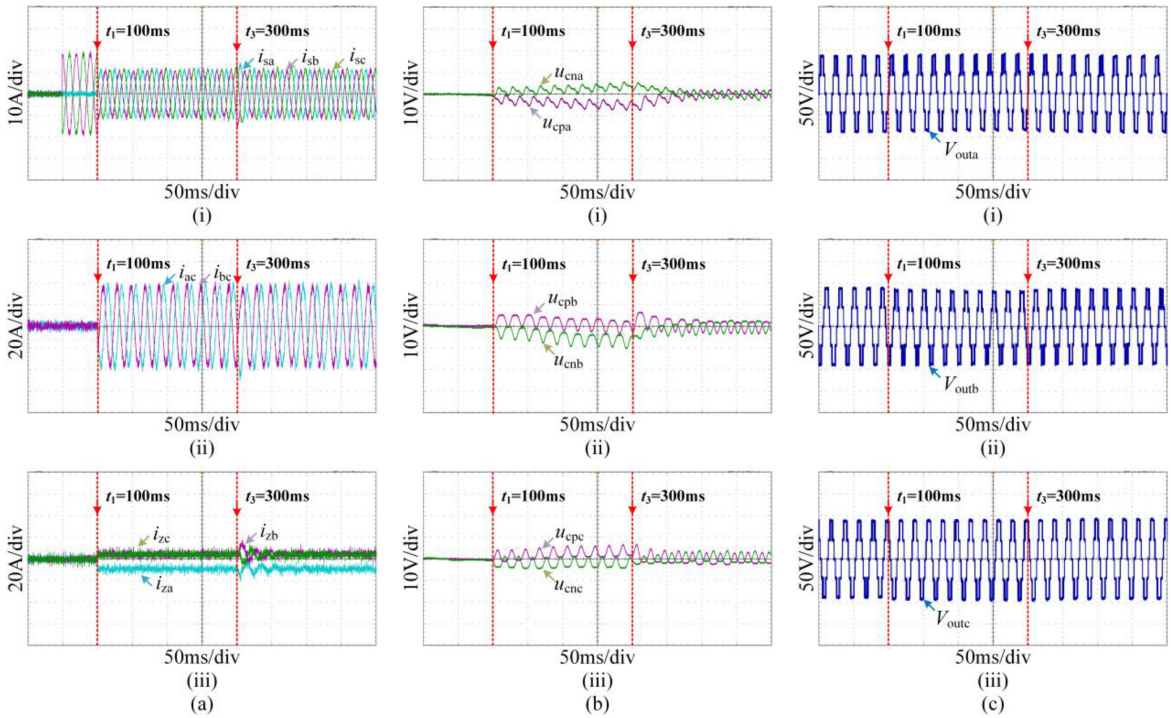

Fig. 13. Experimental results of MMC-SCESS-based RPC in the normal operation mode. (a) Currents: (i) three-phase grid currents, (ii) compensation currents, and (iii) three-phase circulating currents. (b) Three-phase SM capacitor voltages: (i) phase a, (ii) phase b, and (iii) phase c. (c) Three-phase output multilevel voltage: (i) phase a, (ii) phase b, and (iii) phase c.

locomotive. The V/V traction transformer consists of two single-phase transformers and draws the power from the electric grid to the simulated load.

The control system mainly consists of a master controller and a slave controller. First, with the features of high-speed parallel computing for a field-programmable gate array (FPGA) and high-level algorithm tasks for a digital signal processor (DSP), a dual-core controller with the DSP and the FPGA is joined together as a master controller to share computation and execute sophisticated control algorithm. In the master controller, the DSP is mainly responsible for executing the model-predictive control (MPC) method of the MMC, while the FPGA not only executes the balance control methods for SM capacitor voltages and supercapacitor SoC, but also distributes the multiplex pulse signals to control the switching states of SMs. Then, an additional FPGA is distributed in each SM as a slave controller and is responsible for executing the MPC method of the BEC and completing the necessary measurements such as SM capacitor voltages and supercapacitor voltage/current for SoC estimation. Furthermore, the distributed FPGA also ensures the SM protection to prevent overcurrent and overvoltage of the supercapacitor. Both communication data transmit among the controllers and switching signal distribution for SMs are realized through the optical fiber.

The experiments of the MMC-SCESS-based RPC in the normal operation mode are carried out, and the corresponding results are shown in Fig. 13. The load of 5 kW is located at phase b traction power arm, while phase a works on a no-load operation. First, phase b traction locomotive turns into the normal operation mode at $t = 50$ ms without enabling NSC

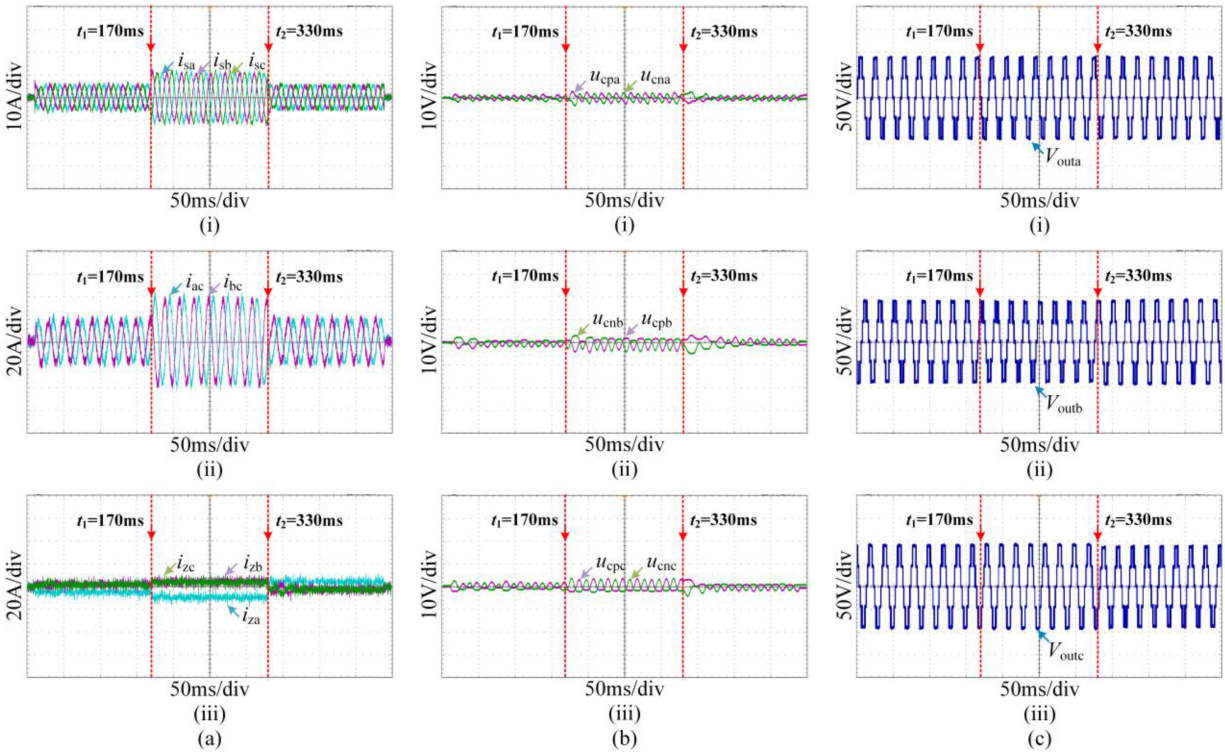

Fig. 14. Experimental results of the MMC without the SCESS-based RPC in the extended operation mode. (a) Currents: (i) three-phase grid currents, (ii) compensation currents, and (iii) three-phase circulating currents. (b) Three-phase SM capacitor voltages: (i) phase a, (ii) phase b, and (iii) phase c. (c) Three-phase output multilevel voltage: (i) phase a, (ii) phase b, and (iii) phase c.

compensation. Three-phase grid currents are seriously asymmetrical and contain a large number of NSCs, as shown in Fig. 13(a)(i). Then, the NSC compensation is enabled at $t = 100$ ms. According to the NSC compensation principle, the reference amplitudes of the active current I_{P} and the reactive current I_{Q} are set to 32.14 and -18.56 A, respectively. According to (14), the reference three-phase circulating currents are -9.26, 4.63, and 4.63 A, respectively. The experimental waveforms of the compensation currents and the circulating currents are shown in Fig. 13(a)(ii) and (a)(iii), respectively. After NSC compensation, three-phase grid currents tend to be symmetrical, and the unbalance level is reduced greatly. Considering that the SM capacitor voltages of the same arm have been balanced by the *sorting algorithm*, it only displays the first SM capacitor voltage of each arm, as shown in Fig. 13(b). It can be seen that the SM capacitor voltages appear to the fundamental and second frequency fluctuations and tend to become divergent in different arms due to the unavoidable power difference. Then, the balance control methods for SM capacitor voltages are applied at $t = 300$ ms. It can be seen that the three-phase circulating currents contain the obvious fundamental components to eliminate the difference between the upper and lower arm voltages, as shown in Fig. 13(a)(iii). The SM capacitor voltages are rebalanced around the reference value of 90 V, and the maximum ripple values of each phase SM capacitor voltages are 4.87, 5.67, and 5.87 V, respectively. Fig. 13(c) shows the three-phase output multilevel voltages. The output voltage level of each phase is up to its maximum value of five. It is worth to mention that the MPC method usually does not require a modulator, so the output multilevel voltage of each phase seems to be irregular. Furthermore, the three-phase output multilevel voltages are also not completely symmetrical. This is due to the characteristic of the asymmetry on the MMC-SCESS-based RPC. The experimental results verify that the MMC-SCESS-based RPC could generate the reference active current and reactive power to compensate the NSC in the normal operation mode and maintain the SM capacitor voltage balance with the balance control methods.

The experiments of the MMC-SCESS-based RPC in the extended operation mode are carried out, and the corresponding results are shown in Figs. 14 and 15, respectively. We assume that phase b traction locomotive first turns into the startup mode at $t = 10$ ms with a constant power of 2.5 kW, then turns into the normal operation mode at $t = 170$ ms with a constant power of 5 kW, and, finally, turns into the braking mode at $t = 330$ ms with a constant power of 2.5 kW.

When the supercapacitor does not work, the startup energy is completely provided by the electric grid, while the regenerative braking energy has to be feedback to the electric grid. In these cases, the NSC compensation has to be enabled to reduce the unbalance of three-phase grid currents, as shown in Fig. 14(a)(i). When the locomotive is operating in the startup mode, the reference amplitudes of the active current I_{P} and the reactive current I_{Q} are set to 16.07 and -9.28 A, respectively. According to (14), the reference three-phase circulating currents are -4.63, 2.32, and 2.32 A, respectively. When the locomotive is operating in the braking mode, the reference amplitudes of the active current

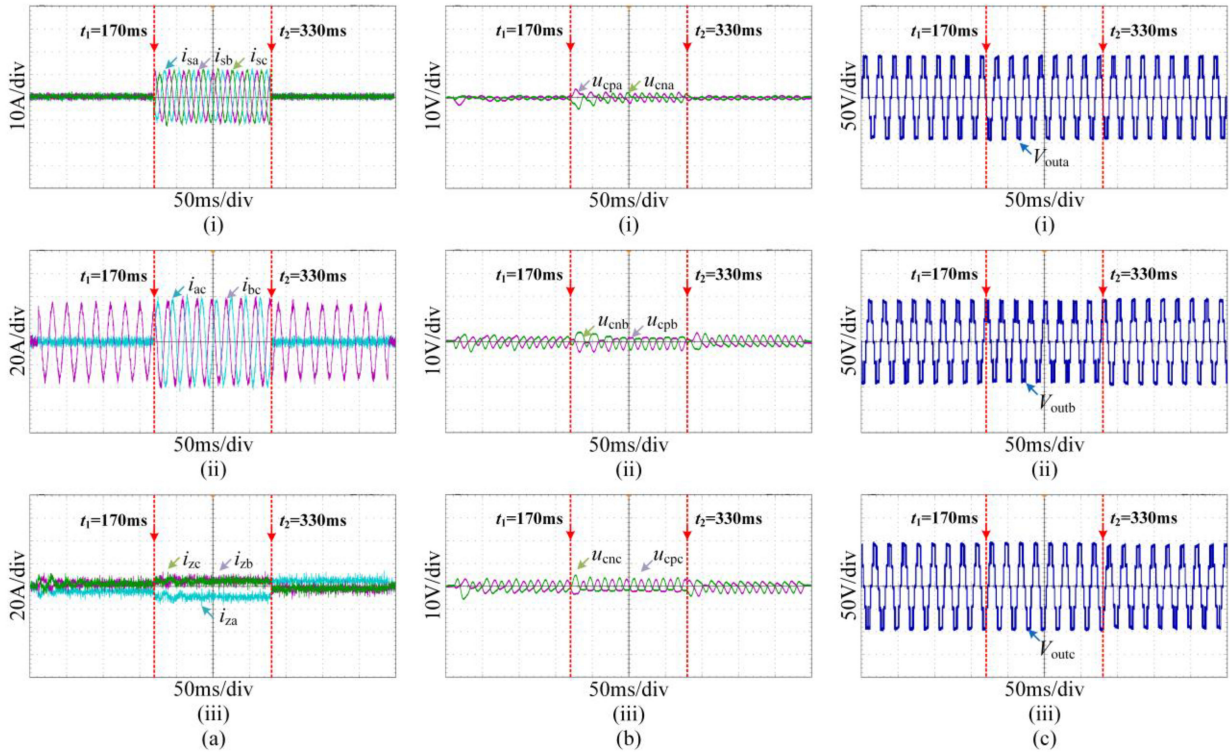

Fig. 15. Experimental results of the MMC with the SCESS-based RPC in the extended operation mode. (a) Currents: (i) three-phase grid currents, (ii) compensation currents, and (iii) three-phase circulating currents. (b) Three-phase SM capacitor voltages: (i) phase a, (ii) phase b, and (iii) phase c. (c) Three-phase output multilevel voltage: (i) phase a, (ii) phase b, and (iii) phase c.

I_{P} and the reactive current I_{Q} are set to -16.07 and 9.28 A, respectively. Also, according to (14), the reference three-phase circulating currents are 4.63, -2.32, and -2.32 A, respectively. The experimental waveforms of the compensation currents and the circulating currents are shown in Fig. 14(a)(ii) and (a)(iii), respectively. Due to the use of balance control method, the SM capacitor voltages of the different arms are well balanced around its reference value of 90 V, as shown in Fig. 14(b). It is worth to mention that the SM capacitor voltage fluctuation under extended operation is smaller than that under normal operation; this is because SM capacitor voltage fluctuation is proportional to the magnitude of the transmission power of the converter [34]. The three-phase output multilevel voltages in the extended mode are not uniformly distributed, which are the same as those in the normal mode, as shown in Fig. 14(c).

When the supercapacitor is access to the dc side of the SM, the startup energy is completely provided by the supercapacitor, while the regenerative braking energy could flow to the supercapacitor via the BEC. In these cases, the effect of the startup mode and the braking mode on the grid current can be neglected, as shown in Fig. 15(a)(i). When the locomotive is operating in the startup mode, the reference amplitude of the active current I_{P} is set to 32.14 A provided by phases b and c together, while the reactive current is not required. To balance the supercapacitor SoC between phase b (phase c) and phase a, additional dc circulating currents are required to be injected in three phases. According to (21), the three-phase reference circulating currents are set to -4.63, 2.32, and 2.32 A, respectively. Similarly, when

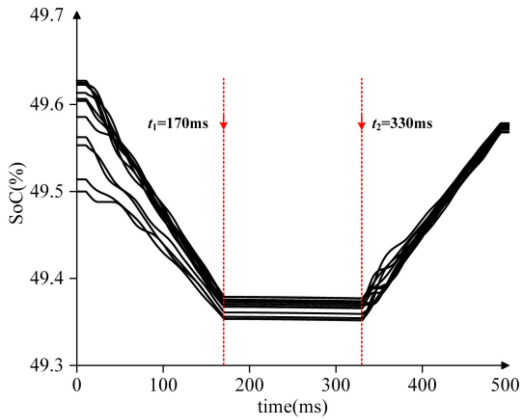

Fig. 16. Three-phase supercapacitors SoC in extended operation mode.

the locomotive is operating in the braking mode, the reference amplitude of the active current I_{P} is set to -32.14 A, and the three-phase reference circulating currents are set to 4.63, -2.32, and -2.32 A, respectively. The experimental waveforms of the compensation currents and three-phase circulating currents are shown in Fig. 15(a)(ii) and (a)(iii), respectively. It is obvious that the BEC could not only provide the bidirectional power flow, but also keep the SM capacitor voltages balanced around the reference value of 90 V. The maximum ripple values of each phase SM capacitor voltages are 2.56, 5.93, and 6.20 V, respectively, in the startup mode and 2.24, 5.53, and 5.66 V, respectively, in

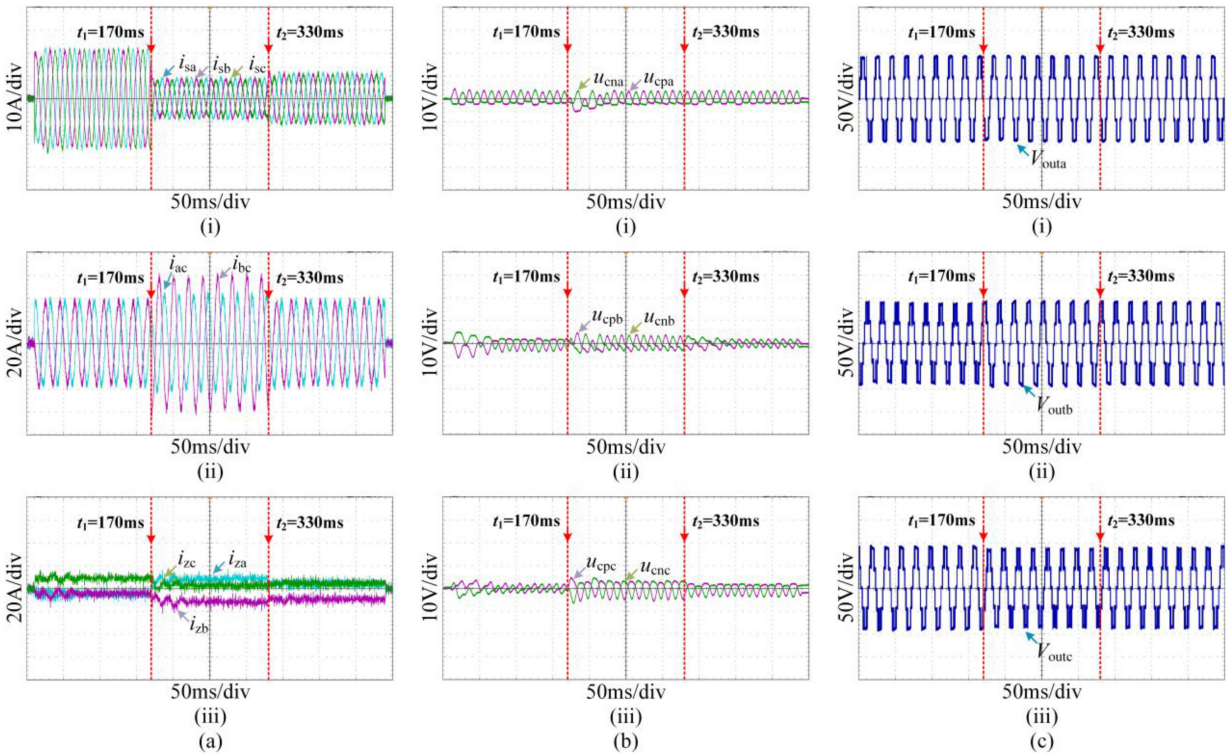

Fig. 17. Experimental results of the MMC with the SCESS-based RPC in the mixed operation mode. (a) Currents: (i) three-phase grid currents, (ii) compensation currents, and (iii) three-phase circulating currents. (b) Three-phase SM capacitor voltages: (i) phase a, (ii) phase b, and (iii) phase c. (c) Three-phase output multilevel voltage: (i) phase a, (ii) phase b, and (iii) phase c.

the braking mode. It is noted that when the MMC-SCESS-based RPC is operating in the extended mode, the SM capacitor voltage fluctuations of phases b and c are significantly larger than those of phase a, as shown in Fig. 15(b); this is because whether the MMC-SCESS is operating in the startup mode or the braking mode, the power interaction occurs among phase b, phase c, and the locomotive directly. The three-phase output multilevel voltages are also not uniformly distributed, as shown in Fig. 15(c). Fig. 16 shows the variation curves of all supercapacitor SoCs of three phases under different operation modes. To verify the SoC balance control methods in the extended mode, the initial imbalance of each supercapacitor is achieved by charging or discharging supercapacitor independently before experiments. When the locomotive is operating in the startup mode, the SoC would be decreased; when the locomotive is operating in the braking mode, the SoC would be increased. Furthermore, all supercapacitor SoCs gradually tend to the same level with the balance control methods. It is worth to mention that when the locomotive is operating in the normal mode, i.e., the supercapacitor does not work, the supercapacitor SoCs still show a slight decrease due to self-discharge.

The experiments of the MMC-SCESS-based RPC in different operation modes at the same time (mixed mode) are carried out, and the corresponding results are shown in Figs. 17 and 18, respectively. We assume that both locomotives A and B turn into the normal mode at $t = 10$ ms with a constant power of 5 kW. Then, locomotive B turns into the braking mode at $t = 170$ ms with a constant power of 2.5 kW, of which 40% flows to locomotive A for power supply and 60% flows to supercapacitor for energy storage. Finally, locomotive B stops operating at $t = 330$ ms.

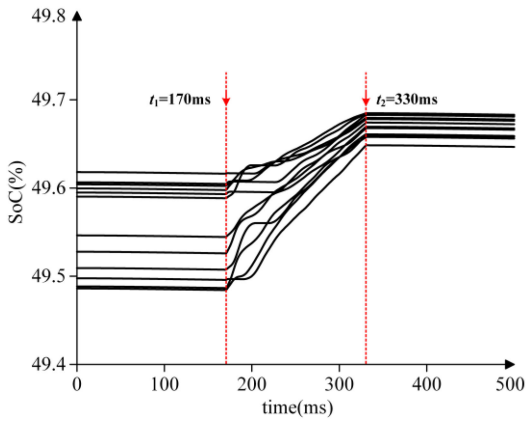

Fig. 18. Three-phase supercapacitors SoC in mixed operation mode.

When locomotive B is operating in the normal mode or the stop mode, the MMC-SCESS-based RPC is mainly responsible for NSC compensation to reduce the unbalance of three-phase grid currents, as shown in Fig. 17(a)(i). When locomotive B is operating in the normal mode, the reference amplitudes of the active current I_{P} and the reactive current I_{Q} are set to 0 and -37.11 A, respectively. According to (14), the reference three-phase circulating currents are -4.63, -4.63, and 9.26 A,

respectively. When locomotive B is operating in the stop mode, the reference amplitudes of the active current I_{P} and the reactive current I_{Q} are set to -32.14 and -18.56 A, respectively. According to (14), the reference three-phase circulating currents are 4.63, -9.26, and 4.63 A, respectively. When locomotive B is operating in the braking mode, the MMC-SCESS-based RPC is responsible for not only NSC compensation, but also regenerative braking energy utilization at the same time. Considering that 40% of braking power (i.e., 1 kW) flows to locomotive A for power supply, the reference amplitudes of the active current I_{P} and the reactive current I_{Q} are set to -38.57 and -14.85 A, respectively. According to (14), the reference three-phase circulating currents are 6.48, -10.19, and 3.70 A, respectively. Considering that 60% of braking power (i.e., 1.5 kW) flows to supercapacitor for energy storage, the reference amplitude of the active current I_{P} is set to -19.28 A provided by phases b and c together. According to (21), the three-phase reference circulating currents are set to 2.78, -1.39, and -1.39 A, respectively. Therefore, after synthesizing the reference values of the above two considerations, the final reference amplitudes of the active current I_{P} and the reactive current I_{Q} provided by phases a and c together are -38.57 and -14.85 A, respectively, and those provided by phases b and c together are -57.85 and -14.85 A, respectively. The final three-phase reference circulating currents are set to 9.26, -11.58, and 2.31 A, respectively. The experimental waveforms of the compensation currents and the circulating currents are shown in Fig. 17(a)(ii) and (a)(iii), respectively. The SM capacitor voltages are well balanced around its reference value of 90 V, as shown in Fig. 17(b). It is worth to mention that the SM capacitor voltages balance in the mixed mode is ensured by the BEC controller. The three-phase output multilevel voltages are also not uniformly distributed, as shown in Fig. 17(c). Fig. 18 shows the variation curves of all supercapacitor SoCs of three phases under different operation modes. Due to a part of the braking power flowing to the supercapacitor in the mixed mode, all supercapacitor SoCs are increased and tend to the same level with the balance control method.

All the above experimental results verify the effectiveness of the proposed current tracking control methods and SoC balance control methods in the extended (or mixed) operation mode.

VI. Conclusion

This paper has investigated an MMC-SCESS for the RPC. In this case, the MMC-SCESS-based RPC could not only provide the ability of NSC compensation, but also achieve the energy storage or energy release for the regenerative braking energy or startup energy of the traction locomotive. First, the mathematical models of the MMC-SCESS-based RPC incorporating the MMC and the BEC are studied. Then, the power flow and the reference circulating current are analyzed and deduced under different operation modes. The balance control methods are presented for the SM capacitor voltage balance and the supercapacitor SoC balance, which are associated with the operation modes. Furthermore, an MPDCC method is also presented for the MMC-SCESS-based RPC to ensure the current tracking performance. Finally, the effectiveness of the investigated MMC-SCESS-based RPC and the proposed control methods is verified by experimental results of a downscaled prototype.

Appendix I

Assuming that the initial phase angle of phase a of the grid side is zero, the initial phase angles of secondary voltages of the V/V transformer are

$$\begin{cases} \theta_{\mathrm{ac}} = -\frac{\pi}{6} \\ \theta_{\mathrm{bc}} = -\frac{\pi}{2}. \end{cases} \tag{Ia}$$

According to (9), the fundamental components of the arm voltage are

$$\begin{cases} \tilde{u}_{\mathrm{a}} = \frac{1}{\sqrt{3}} U_{\mathrm{s}} \sin(\omega t) \\ \tilde{u}_{\mathrm{b}} = \frac{1}{\sqrt{3}} U_{\mathrm{s}} \sin\left(\omega t - \frac{2}{3}\pi\right) \\ \tilde{u}_{\mathrm{c}} = \frac{1}{\sqrt{3}} U_{\mathrm{s}} \sin\left(\omega t - \frac{4}{3}\pi\right). \end{cases} \tag{Ib}$$

The positive-sequence circulating current and the negative circulating current are expressed as

$$\begin{cases} i_{\mathrm{za}+} = I_{\mathrm{z}+} \sin(\omega t + \theta_+) \\ i_{\mathrm{zb}+} = I_{\mathrm{z}+} \sin(\omega t + \theta_+ - 2\pi/3) \\ i_{\mathrm{zc}+} = I_{\mathrm{z}+} \sin(\omega t + \theta_+ - 4\pi/3) \end{cases} \tag{Ic}$$

$$\begin{cases} i_{\mathrm{za}-} = I_{\mathrm{z}-} \sin(\omega t + \theta_-) \\ i_{\mathrm{zb}-} = I_{\mathrm{z}-} \sin(\omega t + \theta_- - 4\pi/3) \\ i_{\mathrm{zc}-} = I_{\mathrm{z}-} \sin(\omega t + \theta_- - 2\pi/3). \end{cases} \tag{Id}$$

The deviations of arm instantaneous power introduced by injecting the circulating currents are shown as

$$\begin{cases} \Delta P_{\mathrm{a}+} = 2\tilde{u}_{\mathrm{a}} i_{\mathrm{za}+} = -\frac{1}{\sqrt{3}} U_{\mathrm{s}} I_{\mathrm{z}+} \left(\cos\left(2\omega t + \theta_+\right) - \cos\theta_+\right) \\ \Delta P_{\mathrm{b}+} = 2\tilde{u}_{\mathrm{b}} i_{\mathrm{zb}+} = -\frac{1}{\sqrt{3}} U_{\mathrm{s}} I_{\mathrm{z}+} \\ \qquad \times \left(\cos\left(2\omega t + \theta_+ - 4\pi/3\right) - \cos\theta_+\right) \\ \Delta P_{\mathrm{c}+} = 2\tilde{u}_{\mathrm{c}} i_{\mathrm{zc}+} = -\frac{1}{\sqrt{3}} U_{\mathrm{s}} I_{\mathrm{z}+} \\ \qquad \times \left(\cos\left(2\omega t + \theta_+ - 2\pi/3\right) - \cos\theta_+\right) \end{cases} \tag{Ie}$$

$$\begin{cases} \Delta P_{\mathrm{a}-} = 2\tilde{u}_{\mathrm{a}} i_{\mathrm{za}-} = -\frac{1}{\sqrt{3}} U_{\mathrm{s}} I_{\mathrm{z}-} \left(\cos\left(2\omega t + \theta_-\right) - \cos\theta_-\right) \\ \Delta P_{\mathrm{b}-} = 2\tilde{u}_{\mathrm{b}} i_{\mathrm{zb}-} = -\frac{1}{\sqrt{3}} U_{\mathrm{s}} I_{\mathrm{z}-} \\ \qquad \times \left(\cos\left(2\omega t + \theta_-\right) - \cos\left(\theta_- - 2\pi/3\right)\right) \\ \Delta P_{\mathrm{c}-} = 2\tilde{u}_{\mathrm{c}} i_{\mathrm{zc}-} = -\frac{1}{\sqrt{3}} U_{\mathrm{s}} I_{\mathrm{z}-} \\ \qquad \times \left(\cos\left(2\omega t + \theta_-\right) - \cos\left(\theta_- - 4\pi/3\right)\right). \end{cases} \tag{If}$$

According to (Ie) and (If), the deviations of arm active power introduced by injecting the circulating currents are given as

$$\begin{cases} P_{\mathrm{diffa}} = \Delta\bar{P}_{\mathrm{a}+} + \Delta\bar{P}_{\mathrm{a}-} = \frac{1}{\sqrt{3}} U_{\mathrm{s}} I_{\mathrm{z}+} \cos\theta_+ + \frac{1}{\sqrt{3}} U_{\mathrm{s}} I_{\mathrm{z}-} \cos\theta_- \\ P_{\mathrm{diffb}} = \Delta\bar{P}_{\mathrm{b}+} + \Delta\bar{P}_{\mathrm{b}-} = \frac{1}{\sqrt{3}} U_{\mathrm{s}} I_{\mathrm{z}+} \cos\theta_+ \\ \qquad + \frac{1}{\sqrt{3}} U_{\mathrm{s}} I_{\mathrm{z}-} \cos\left(\theta_- - 2\pi/3\right) \\ P_{\mathrm{diffc}} = \Delta\bar{P}_{\mathrm{c}+} + \Delta\bar{P}_{\mathrm{c}-} = \frac{1}{\sqrt{3}} U_{\mathrm{s}} I_{\mathrm{z}+} \cos\theta_+ \\ \qquad + \frac{1}{\sqrt{3}} U_{\mathrm{s}} I_{\mathrm{z}-} \cos\left(\theta_- - 4\pi/3\right). \end{cases} \tag{Ig}$$

APPENDIX II

$$\boldsymbol{A}=\begin{bmatrix}-\frac{r}{L} & 0\\ 0 & -\frac{r}{L}\end{bmatrix},$$

$$\boldsymbol{B}=\begin{bmatrix}-\frac{u^{\Sigma}_{\mathrm{pc}j}}{NL}N_{\mathrm{p}}+\frac{u^{\Sigma}_{\mathrm{nc}j}}{NL}N_{n}-\frac{2}{L}\left(u_{j\mathrm{c}}-u_{\mathrm{co}}\right)\\ -\frac{u^{\Sigma}_{\mathrm{pc}j}}{2NL}N_{\mathrm{p}}-\frac{u^{\Sigma}_{\mathrm{nc}j}}{2NL}N_{\mathrm{n}}+\frac{1}{2L}U_{\mathrm{dc}}\end{bmatrix}$$

$$\boldsymbol{A'}=\begin{bmatrix}0 & -\frac{Q}{C_{\mathrm{sm}}}\\ \frac{Q}{L_{\mathrm{s}}} & -\frac{r_{\mathrm{s}}}{L_{\mathrm{s}}}\end{bmatrix},\ \boldsymbol{B'}=\begin{bmatrix}\frac{i_{\mathrm{e}}}{C_{\mathrm{sm}}}\\ -\frac{u_{\mathrm{sup}}}{L_{\mathrm{s}}}\end{bmatrix}$$

$$\boldsymbol{G}=\begin{bmatrix}1-\frac{r}{L}T_{\mathrm{s}} & 0\\ 0 & 1-\frac{r}{L}T_{\mathrm{s}}\end{bmatrix}$$

$$\boldsymbol{H}=\begin{bmatrix}-\frac{u^{\Sigma}_{\mathrm{pc}j}}{NL}N_{\mathrm{p}}T_{\mathrm{s}}+\frac{u^{\Sigma}_{\mathrm{nc}j}}{NL}N_{\mathrm{n}}T_{\mathrm{s}}-\frac{2}{L}\left(u_{j\mathrm{c}}-u_{\mathrm{co}}\right)T_{\mathrm{s}}\\ -\frac{u^{\Sigma}_{\mathrm{pc}j}}{2NL}N_{\mathrm{p}}T_{\mathrm{s}}-\frac{u^{\Sigma}_{\mathrm{nc}j}}{2NL}N_{\mathrm{n}}T_{\mathrm{s}}+\frac{1}{2L}U_{\mathrm{dc}}T_{\mathrm{s}}\end{bmatrix}$$

$$\boldsymbol{G'}=\begin{bmatrix}1 & -\frac{Q}{C_{\mathrm{sm}}}T_{\mathrm{s}}\\ \frac{Q}{L_{\mathrm{s}}}T_{\mathrm{s}} & 1-\frac{r_{\mathrm{s}}}{L_{\mathrm{s}}}T_{\mathrm{s}}\end{bmatrix},\ \boldsymbol{H'}=\begin{bmatrix}\frac{i_{\mathrm{e}}}{C_{\mathrm{sm}}}T_{\mathrm{s}}\\ -\frac{u_{\mathrm{sup}}}{L_{\mathrm{s}}}T_{\mathrm{s}}\end{bmatrix}.$$

REFERENCES

[1] S. M. M. Gazafrudi, A. T. Langerudy, E. F. Fuchs, and K. al-Haddad, "Power quality issues in railway electrification: A comprehensive perspective," *IEEE Trans. Ind. Electron.*, vol. 62, no. 5, pp. 3081–3090, May 2015.

[2] H. Hu, Z. He, X. Li, K. Wang, and S. Gao, "Power-quality impact assessment for high-speed railway associated with high-speed trains using train timetable—Part I: Methodology and modeling," *IEEE Trans. Power Del.*, vol. 31, no. 2, pp. 693–703, Apr. 2016.

[3] H. Hu, Z. He, K. Wang, X. Ma, and S. Gao, "Power-quality impact assessment for high-speed railway associated with high-speed trains using train timetable—Part II: Verifications, estimations and applications," *IEEE Trans. Power Del.*, vol. 31, no. 4, pp. 1482–1492, Apr. 2016.

[4] S. Hu *et al.*, "A new railway power flow control system coupled with asymmetric double LC branches," *IEEE Trans. Power Electron.*, vol. 30, no. 10, pp. 5484–5498, Oct. 2015.

[5] H. Hayashiya *et al.*, "Review of regenerative energy utilization in traction power supply system in Japan: Applications of energy storage systems in d.c. traction power supply system," in *Proc. 43th Annu. Conf. IEEE Ind. Electron. Soc.*, Nov. 2017, pp. 3918–3923.

[6] Z. Zhang, B. Wu, J. Kang, and L. Luo, "A multi-purpose balanced transformer for railway traction applications," *IEEE Trans. Power Del.*, vol. 24, no. 2, pp. 711–718, Apr. 2009.

[7] A. A. Badin and I. Barbi, "Unity power factor isolated three-phase rectifier with two single-phase buck rectifiers based on the Scott transformer," *IEEE Trans. Power Electron.*, vol. 26, no. 9, pp. 2688–2696, Sep. 2011.

[8] C. Zhao *et al.*, "Design, implementation and performance of a modular power electronic transformer (PET) for railway application," in *Proc. 14th Eur. Conf. Power Electron. Appl.*, Birmingham, U.K., 2011, pp. 1–10.

[9] G. P. Zhu, J. Y. Chen, and X. Y. Liu, "Compensating for the negative sequence currents of electric railway based on SVC," in *Proc. 3rd IEEE Conf. Ind. Electron. Appl.*, Jun. 2008, pp. 1958–1963.

[10] G. Celli, F. Pilo, and S. B. Tennakoon, "Voltage regulation on 25 kV AC railway systems by using thyristor switched capacitor," in *Proc. 9th Int. Conf. Harmon. Qual. Power*, 2000, vol. 2, pp. 633–638.

[11] K. Fujii *et al.*, "STATCOM applying flat-packaged IGBTs connected in series," *IEEE Trans. Power Electron.*, vol. 20, no. 5, pp. 1125–1132, Sep. 2005.

[12] R Grunbaum, J. -Ph. Hasler, T. Larsson, and M. Meslay, "STATCOM to enhance power quality and security of rail traction supply," in *Proc. 8th Int. Symp. Adv. ElectroMech. Motion Syst. Elect. Drives*, 2009, pp. 1–6.

[13] S. Hu *et al.*, "A new integrated hybrid power quality control system for electrical railway," *IEEE Trans. Ind. Electron.*, vol. 62, no. 10, pp. 6222–6232, Oct. 2015.

[14] K. W. Lao, M. C. Wong, N. Y. Dai, C. K. Wong, and C.-S. Lam, "A systematic approach to hybrid railway power conditioner design with harmonic compensation for high-speed railway," *IEEE Trans. Ind. Electron.*, vol. 62, no. 2, pp. 930–942, Feb. 2015.

[15] Y. Mochinaga, M. Takeda, and K. Hasuike, "Static power conditioner using GTO converters for ac electric railway," in *Proc. Conf. Rec. Power Convers. Conf.*, Yokohama, Japan, Apr. 1993, pp. 641–646.

[16] Y. Horita, N. Morishima, M. Kai, M. Onishi, T. Masui, and M. Noguchi, "Single-phase STATCOM for feeding system of Tokaido Shinkansen," in *Proc. Int. Power Electron. Conf.*, 2010, pp. 2165–2170.

[17] F. Ma *et al.*, "A railway traction power conditioner using modular multilevel converter and its control strategy for high-speed railway system," *IEEE Trans. Transp. Electrif.*, vol. 2, no. 1, pp. 96–109, Mar. 2016.

[18] X. Tian, Q. R. Jiang, Y. D. Wei, J. M. Zhang, and Y. T. Wei, "Novel high-speed railway uninterruptible flexible connector based on modular multilevel converter structure," in *Proc. 9th Int. Conf. Power Electron. ECCE Asia*, Seoul, South Korea, Jun. 1–5, 2015, pp. 952–958.

[19] W. Wang and W. Gui, "Study on harmonic suppression technology of electrified railway based on MRPC," *Elect. Drive Locomotives*, no. 2, pp. 21–30, 2014.

[20] S. Song, J. Liu, S. Ouyang, and X. Chen, "A modular multilevel converter based railway power conditioner for power balance and harmonic compensation in Scott railway traction system," in *Proc. 8th Int. Power Electron. Motion Control Conf.*, 2016, vol. 1, pp. 2412–2416.

[21] Q. Xu *et al.*, "Analysis and comparison of modular railway power conditioner for high-speed railway traction system," *IEEE Trans. Power Electron.*, vol. 32, no. 8, pp. 6031–6048, Aug. 2017.

[22] P. F. Ribeiro, B. K. Johnson, M. L. Crow, A. Arsoy, and Y. Liu, "Energy storage systems for advanced power applications," *Proc. IEEE*, vol. 89, no. 12, pp. 1744–1756, Dec. 2001.

[23] T. Soong and P. Lehn, "Evaluation of emerging modular multilevel converters for BESS applications," *IEEE Trans. Power Del.*, vol. 29, no. 5, pp. 2086–2094, Oct. 2014.

[24] I. Trintis, S. Munk-Nielsen, and R. Teodorescu, "A new modular multilevel converter with integrated energy storage," in *Proc. 37th Annu. Conf. IEEE Ind. Electron. Soc.*, Nov. 7–10, 2011, pp. 1075–1080.

[25] J. I. Y. Ota, T. Sato, and H. Akagi, "Enhancement of performance, availability, and flexibility of a battery energy storage system based on a modular multilevel cascaded converter (MMCC-SSBC)," *IEEE Trans. Power Electron.*, vol. 31, no. 4, pp. 2791–2799, Apr. 2016.

[26] A. Lachichi, "On modular multilevel converters-based batteries energy storage systems," in *Proc. IEEE Int. Conf. Power Electron. Drive Syst.*, 2015, pp. 908–912.

[27] M. Vasiladiotis and A. Rufer, "Analysis and control of modular multilevel converters with integrated battery energy storage," *IEEE Trans. Power Electron.*, vol. 30, no. 1, pp. 163–175, Jan. 2015.

[28] N. Li, F. Gao, T. Hao, Z. Ma, and C. Zhang, "SOH balancing control method for the MMC battery energy storage system," *IEEE Trans. Ind. Electron.*, vol. 65, no. 8, pp. 6581–6591, Aug. 2018.

[29] A. Hillers, M. Stojadinovic, and J. Biela, "Systematic comparison of modular multilevel converter topologies for battery energy storage systems based on split batteries," in *Proc. 17th Eur. Conf. Power Electron. Appl.*, Sep. 2015, pp. 1–9.

[30] Q. Chen, R. Li, and X. Cai, "Analysis and fault control of hybrid modular multilevel converter with integrated battery energy storage system," *IEEE J. Emerg. Sel. Topics Power Electron.*, vol. 5, no. 1, pp. 64–78, Mar. 2017.

[31] L. Zhang, Y. Tang, S. Yang, and F. Gao, "Decoupled power control for a modular multilevel converter-based hybrid AC-DC grid integrated with hybrid energy storage," *IEEE Trans. Ind. Electron.*, vol. 66, no. 4, pp. 2926–2934, Apr. 2019, doi: 10.1109/TIE.2018.2842795.

[32] D. Iannuzzi and P. Tricoli, "Speed-based state-of-charge tracking control for metro trains with onboard supercapacitors," *IEEE Trans. Power Electron.*, vol. 27, no. 4, pp. 2129–2140, Apr. 2012.

[33] M. Coppola, A. Del Pizzo, and D. Iannuzzi, "A power traction converter based on modular multilevel architecture integrated with energy storage devices," in *Proc. 2nd Int. Conf. Elect. Syst. Aircr. Railway Ship Propulsion*, Bologna, Italy, Oct. 16–18, pp. 1–7.

[34] K. Sharifabadi, L. Harnefors, H. Nee, S. Norrga, and R. Teodorescu, *Design, Control and Application of Modular Multilevel Converters for HVDC Transmission Systems*. New York, NY, USA: Wiley, 2016, ch. 3, pp. 135–145.

[35] L. Harnefors, A. Antonopoulos, S. Norrga, L. Ängquist, and H.-P. Nee, "Dynamic analysis of modular multilevel converters," *IEEE Trans. Ind. Electron.*, vol. 60, no. 7, pp. 2526–2537, Jul. 2013.
[36] F. Ma, A. Luo, X. Xu, H. Xiao, C. Wu, and W. Wang, "A simplified power conditioner based on half-bridge converter for high-speed railway system," *IEEE Trans. Ind. Electron.*, vol. 60, no. 2, pp. 728–738, Feb. 2013.
[37] A. Hassanpoor, L. Angquist, S. Norrga, K. Ilves, and H. P. Nee, "Tolerance band modulation methods for modular multilevel converters," *IEEE Trans. Power Electron.*, vol. 30, no. 1, pp. 311–326, Jan. 2015.
[38] J. Rodriguez and P. Cortes, *Predictive Control of Power Converters and Electrical Drives*. Hoboken, NJ, USA: Wiley, 2012.
[39] P. Cortes, A. Wilson, S. Kouro, J. Rodriguez, and H. Abu-Rub, "Model predictive control of multilevel cascaded H-bridge inverters," *IEEE Trans. Ind. Electron.*, vol. 57, no. 8, pp. 2691–2699, Aug. 2010.
[40] Z. Gong, P. Dai, X. Yuan, X. Wu, and G. Guo, "Design and experimental evaluation of fast model predictive control for modular multilevel converters," *IEEE Trans. Ind. Electron.*, vol. 63, no. 6, pp. 3845–3856, Jun. 2016.
[41] B. Gutierrez and S. Kwak, "Modular multilevel converters (MMCs) controlled by model predictive control with reduced calculation burden," *IEEE Trans. Power Electron.*, vol. 33, no. 11, pp. 9176–9187, Nov. 2018.

Peng Guo (S'18) was born in Hunan, China, in 1992. He received the B.S. degree in electrical engineering from the Wuhan University of Technology, Wuhan, China, in 2015. He is currently working toward the Ph.D. degree in electrical engineering with the College of Electrical and Information Engineering, Hunan University, Changsha, China.

His main research interests include modular multilevel converters and model-predictive control and its applications in power electronics.

Qianming Xu (M'17) was born in Henan, China, in 1989. He received the B.S. degree in electrical engineering and automation and the Ph.D. degree in electrical engineering from Hunan University, Changsha, China, in 2012 and 2017, respectively.

Since 2019, he has been an Associate Professor with the College of Electrical and Information Engineering, Hunan University. His research interests include modular multilevel converters, power quality control, and dc grid control.

Yufei Yue (S'16) was born in Henan, China, in 1991. She received the B.S. degree in electrical engineering and automation in 2014 from the College of Electrical and Information Engineering, Hunan University, Changsha, China, where she is working toward the Ph.D. degree in electrical engineering.

Her research interests include modular multilevel converters and power quality control.

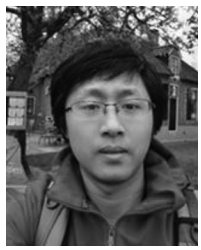

Fujun Ma (M'15) was born in Hunan, China, in 1985. He received the B.S. degree in automation and the Ph.D. degree in electrical engineering from Hunan University, Changsha, China, in 2008 and 2015, respectively.

Since 2016, he has been an Associate Professor with the College of Electrical and Information Engineering, Hunan University. His research interests include the power quality managing technique of electrified railway, electric power saving, reactive power compensation, and active power filters.

Zhixing He (M'17) was born in Hunan, China, in 1989. He received the B.S. degree in information science and engineering from Central South University, Changsha, China, in 2011, and the Ph.D. degree in electrical engineering from Hunan University, Changsha, in 2017.

Between 2017 and 2018, he was a Postdoctoral Researcher with Hunan University, where he is currently an Associate Professor with the College of Electrical and Information Engineering. His research interests include power electronics, medium-voltage dc systems, model-predictive control, and modular multilevel converters.

An Luo (SM'09) was born in Changsha, China, in 1957. He received the B.S. and M.S. degrees in industrial automation from Hunan University, Changsha, in 1982 and 1986, respectively, and the Ph.D. degree in fluid power transmission and control from Zhejiang University, Hangzhou, China, in 1993.

Between 1996 and 2002, he was a Professor with Central South University, Changsha. Since 2003, he has been a Professor with the College of Electrical and Information Engineering, Hunan University, where he also serves as the Chief of National Electric Power Conversion and Control Engineering Technology Research Center. His research interests mainly include distributed generation, microgrids, and power quality.

Dr. Luo was elected to the Chinese National Academy of Engineering in 2015, the highest honor for scientists, engineers, and scientists in China. He has received the highly prestigious China National Science and Technology Awards three times in 2006, 2010, and 2014.

Josep M. Guerrero (S'01–M'04–SM'08–F'15) received the B.S. degree in telecommunications engineering, the M.S. degree in electronics engineering, and the Ph.D. degree in power electronics from the Technical University of Catalonia, Barcelona, Spain, in 1997, 2000, and 2003, respectively.

Since 2011, he has been a Full Professor with the Department of Energy Technology, Aalborg University, Aalborg, Denmark. Since 2015, he has been a Distinguished Guest Professor with Hunan University, Changsha, China. His research interests mainly include power electronics, distributed energy storage, and microgrids.

Prof. Guerrero is an Associate Editor for the IEEE TRANSACTIONS ON POWER ELECTRONICS, the IEEE TRANSACTIONS ON INDUSTRIAL ELECTRONICS, and the IEEE INDUSTRIAL ELECTRONICS MAGAZINE, and an Editor for the IEEE TRANSACTIONS ON SMART GRID and the IEEE TRANSACTIONS ON ENERGY CONVERSION. In 2014, 2015, and 2016, he was awarded by Thomson Reuters as the Highly Cited Researcher.